

# ResearchOnline@JCU

This file is part of the following reference:

**Fay, C. (2014) *Modeling, describing, measuring and interpreting porphyroblast inclusion trails to understand inter-relationships between deformation, metamorphism and tectonism*. PhD thesis, James Cook University.**

Access to this file is available from:

<http://researchonline.jcu.edu.au/39976/>

*The author has certified to JCU that they have made a reasonable effort to gain permission and acknowledge the owner of any third party copyright material included in this document. If you believe that this is not the case, please contact*

*[ResearchOnline@jcu.edu.au](mailto:ResearchOnline@jcu.edu.au) and quote  
<http://researchonline.jcu.edu.au/39976/>*

**MODELING, DESCRIBING, MEASURING AND INTERPRETING  
PORPHYROBLAST INCLUSION TRAILS TO UNDERSTAND INTER-  
RELATIONSHIPS BETWEEN DEFORMATION, METAMORPHISM  
AND TECTONISM**

**Volume II**

**(Figures)**

**Thesis submitted by**

**C.Fay, Bsc Université Lyon I,**

**Msc ENS Lyon – Université Nice Sophia Antipolis, France.**

**In November 2014**

**For the degree of Doctor of Philosophy**

**in the College of Science, Technology and Engineering**

**James Cook University**

---

## CONTENT OF VOLUME II

List of Figures.....	ii-iv
<b>-CHAPTER I-</b> .....	<b>p1-6</b>
<i>Porphyroblast rotation versus non-rotation: conflict resolution!</i>	
<b>-CHAPTER II-</b> .....	<b>p7-31</b>
<i>Polyphase tectonism and orocline development revealed by spatial shifts in deformation partitioning</i>	
<b>-CHAPTER III-</b> .....	<b>p32-46</b>
<i>Inclusion trail analysis techniques, multiply interleaved growth of staurolite and andalusite, and shifting of reaction vs deformation with time</i>	
<b>-CHAPTER IV-</b> .....	<b>p47-69</b>
<i>The significance for metamorphism, orogenesis and PT paths of ~40 million years of multiple phases of deformation and effectively synchronous staurolite-andalusite growth</i>	

---

**LIST OF FIGURES**

**-CHAPTER I-**

Figure 1 .....p2  
Figure 2 .....p3  
Figure 3 .....p4  
Figure 4.....p5  
Figure 5.....p6

**-CHAPTER II-**

Figure 1.....p8  
Figure 2.....p9  
Figure 3.....p10  
Figure 4.....p11  
Figure 5.....p12  
Figure 6.....p13-14  
Figure 7.....p15-16  
Figure 8.....p17  
Figure 9.....p18  
Figure 10.....p19  
Figure 11.....p20  
Figure 12.....p21  
Figure 13.....p22  
Figure 14.....p23  
Figure 15.....p24  
Figure 16.....p25-26  
Figure 17.....p27

---

Figure 18.....	p28
Figure 19.....	p29
Figure 20.....	p30
Figure 21.....	p31
<b>-CHAPTER III-</b>	
Figure 1.....	p33
Figure 2a.....	p34
Figure 2b.....	p35
Figure 2c.....	p36
Figure 3a, b, c, b.....	p37
Figure 3e, f, g, h.....	p38
Figure 4a,b.....	p39
Figure 4c.....	p40
Figure 5.....	p41
Figure 6.....	p42
Figure 7.....	p43
Figure 8.....	p44
Figure 9.....	p45
Figure 10.....	p46
<b>-CHAPTER IV-</b>	
Figure 1.....	p48-49
Figure 2.....	p50
Figure 3.....	p51
Figure 4.....	p52
Figure 5.....	p53

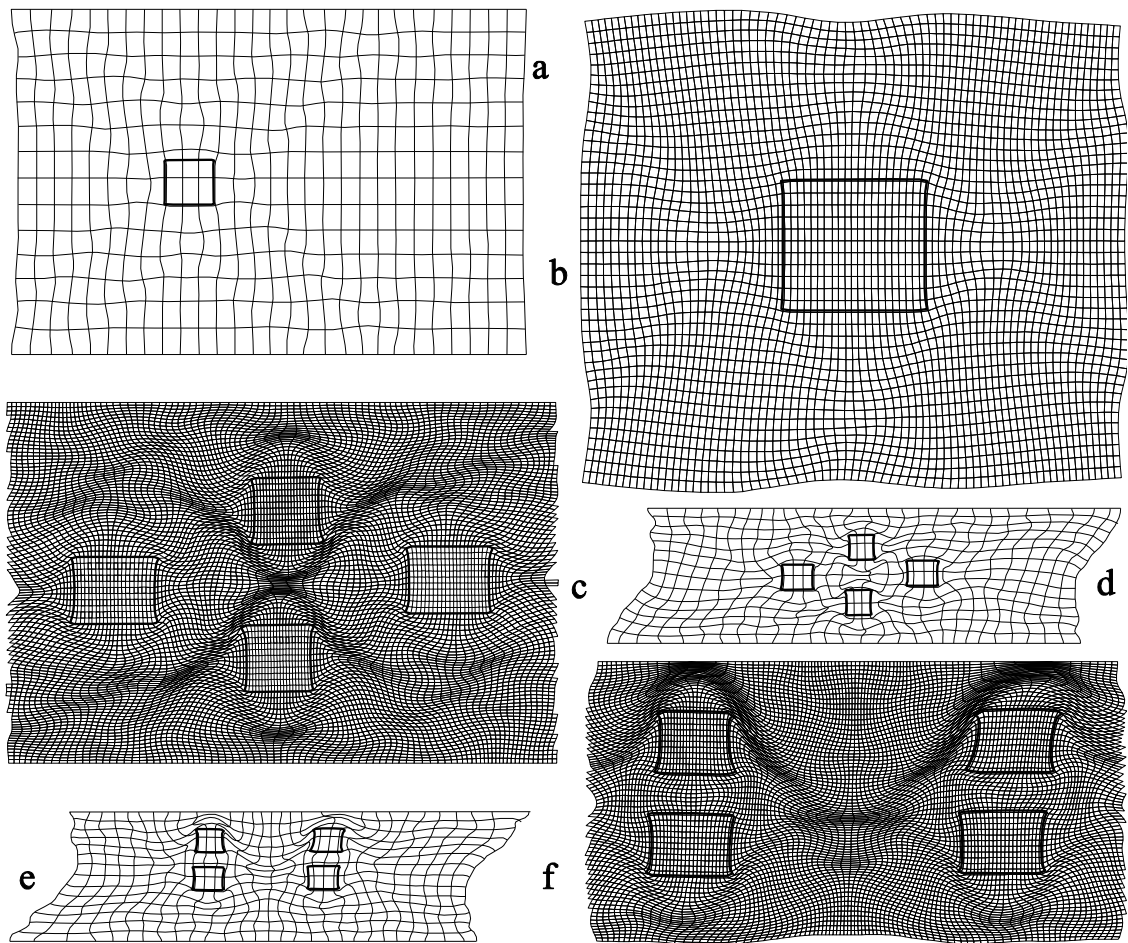
---

Figure 6.....	p54-55
Figure 7.....	p56
Figure 8.....	p57
Figure 9.....	p57
Figure 10a.....	p58
Figure 10b.....	p59
Figure 11.....	p60-61
Figure 12.....	p62-63
Figure 13.....	p64
Figure 14.....	p65-66
Figure 15a & b.....	p67
Figure 15c.....	p68
Figure 16.....	p69

**- CHAPTER I –**

**PORPHYROBLAST ROTATION VERSUS NON-ROTATION:**

**CONFLICT RESOLUTION!**



**Figure 1:** The anastomosing millipede geometry produced around a porphyroblast produced by (a, b) 35% bulk shortening. (c, d) the effect of combined shortening and shearing after millipede geometries had been first produced by 50% of bulk shortening. (e, f) the effect of shearing only after millipede geometries had been first produced by 50% of bulk shortening.

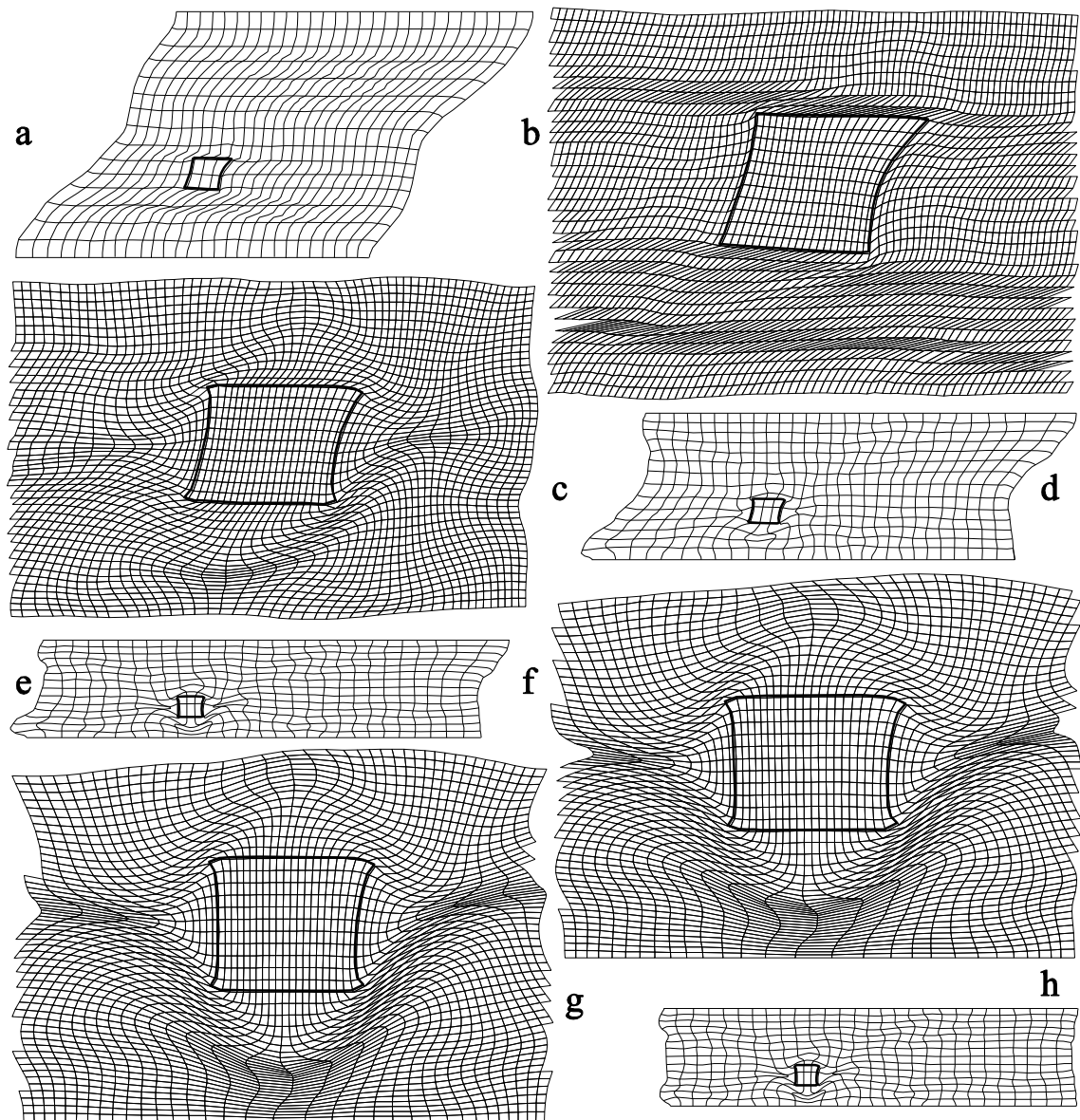


**Figure 2:** The effects of progressive shearing only on a millipede geometry developed by various amounts of initial shortening (a, b) 15% of shortening, (c, d) 40% of shortening, (e, f) 60% of shortening. (g, h) shows the millipede geometry developed prior to commencing shearing shown in (e, f). Each pair shows a simplified strain field for the full model plus the detailed strain field around the porphyroblast.

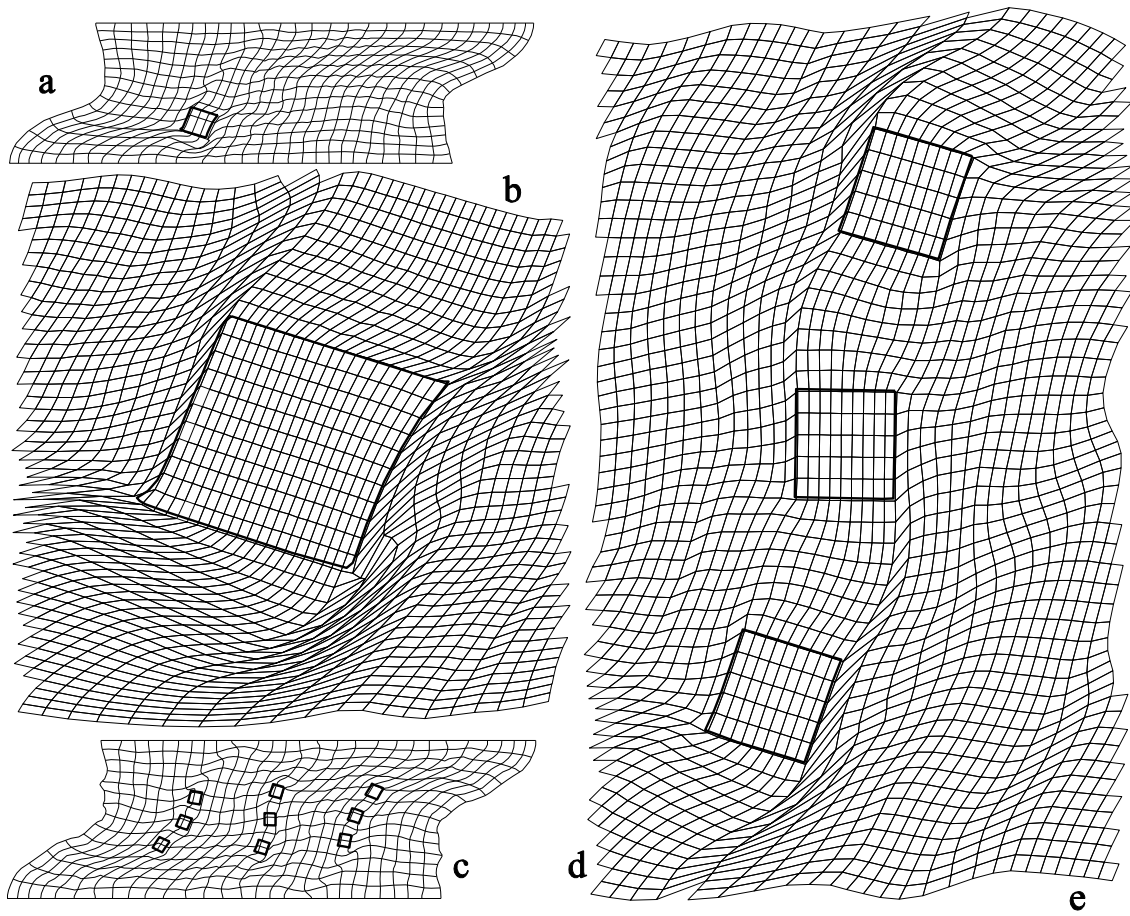


**Figure 3:** Effects of synchronous bulk shortening and shearing on 1( a and b) versus 9 (c and d) porphyroblasts without the first developing a millipede microstructure.

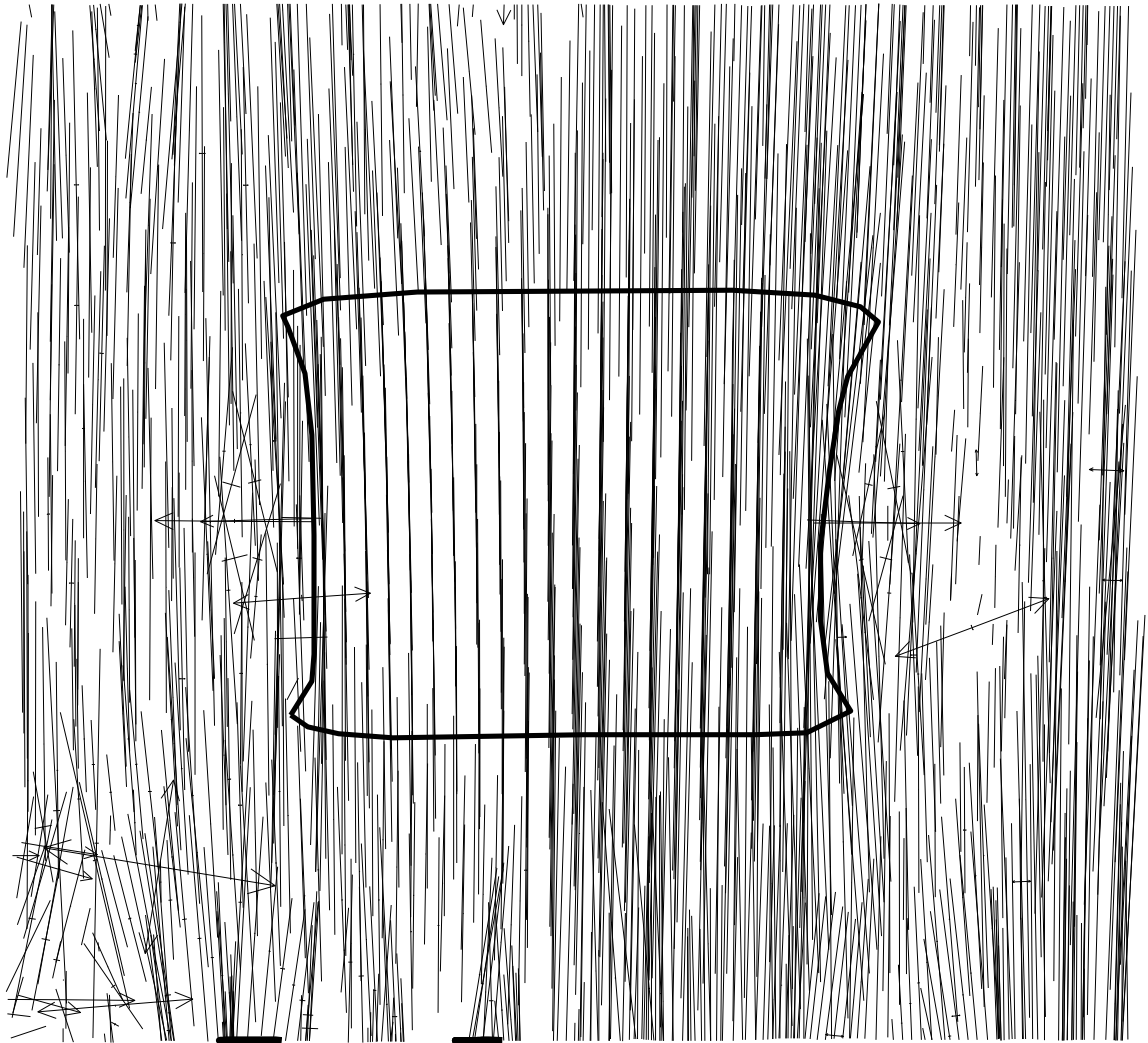


**Figure 4:** Detail of the stress field around the porphyroblast shown in Figures 2e and 2f. Each subvertical line represents the local orientation of  $\sigma_1$ . The gently dipping lines with arrowheads indicate deviatoric tension.

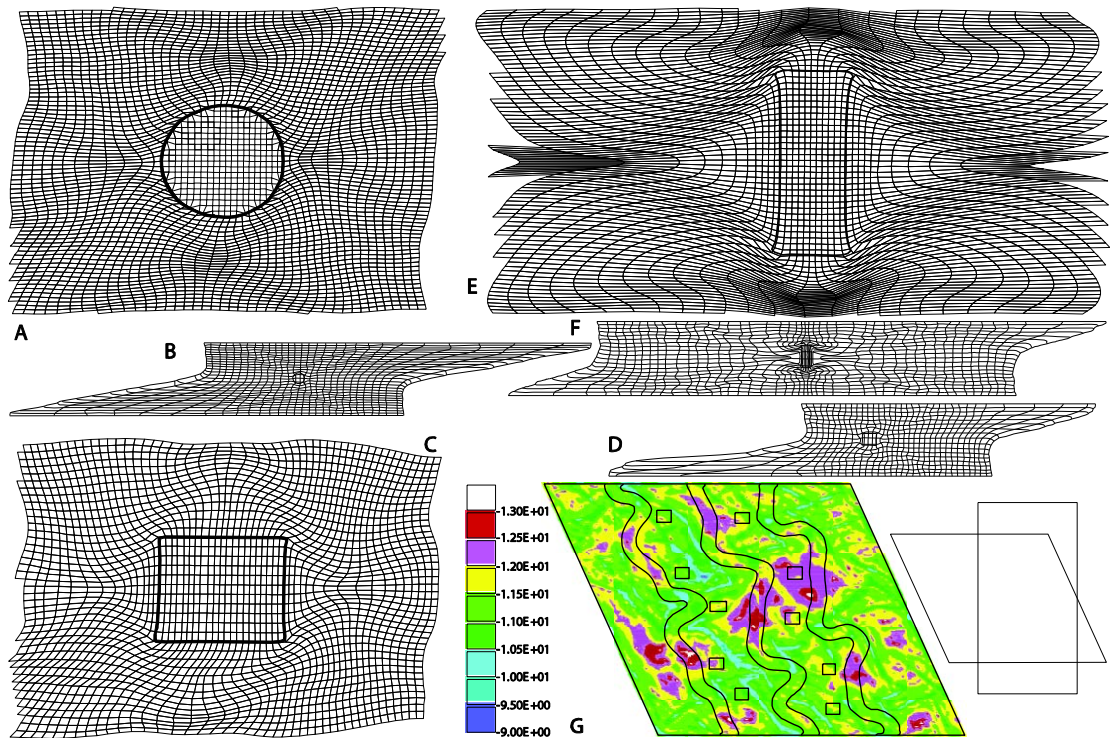


**Figure 5:** (a-f) Simplified strain field for the full model plus detail around “porphyroblasts”. Effects of shearing only (fixed velocity applied to the top and bottom with these constrained to remain straight and parallel; sides are free) after millipede geometries were developed by bulk shortening of a sphere (a, b), rectangle (c, d) and square (e, f) by 20, 50 and 20% shortening respectively. (g) “Porphyroblasts” and contoured logarithm of strain rate resulting from constant velocity parallel to initially vertical layers coupled with simple shearing normal to this direction. The horizontal velocity was adjusted to maintain an isochoric deformation. This elastic-viscous material can undergo both strain and strain-rate softening with the viscosity at strain-rate  $\dot{\epsilon}$  given by  $\eta = \eta_0 \epsilon^p \left( \frac{\dot{\epsilon}_0}{\dot{\epsilon}} \right)^q$  where  $\eta$  is the current viscosity,  $\eta_0$  is the viscosity at a reference strain-rate  $\dot{\epsilon}_0$ , and  $p, q$  are strain and strain-rate softening parameters ( $p=-0.8$  and  $q=2.0$ ; initial viscosity ratio between layers and embedding medium is 10).

**- CHAPTER II -**

**POLYPHASE TECTONISM AND OROCLINE DEVELOPMENT  
REVEALED BY SPATIAL SHIFTS IN DEFORMATION  
PARTITIONING**

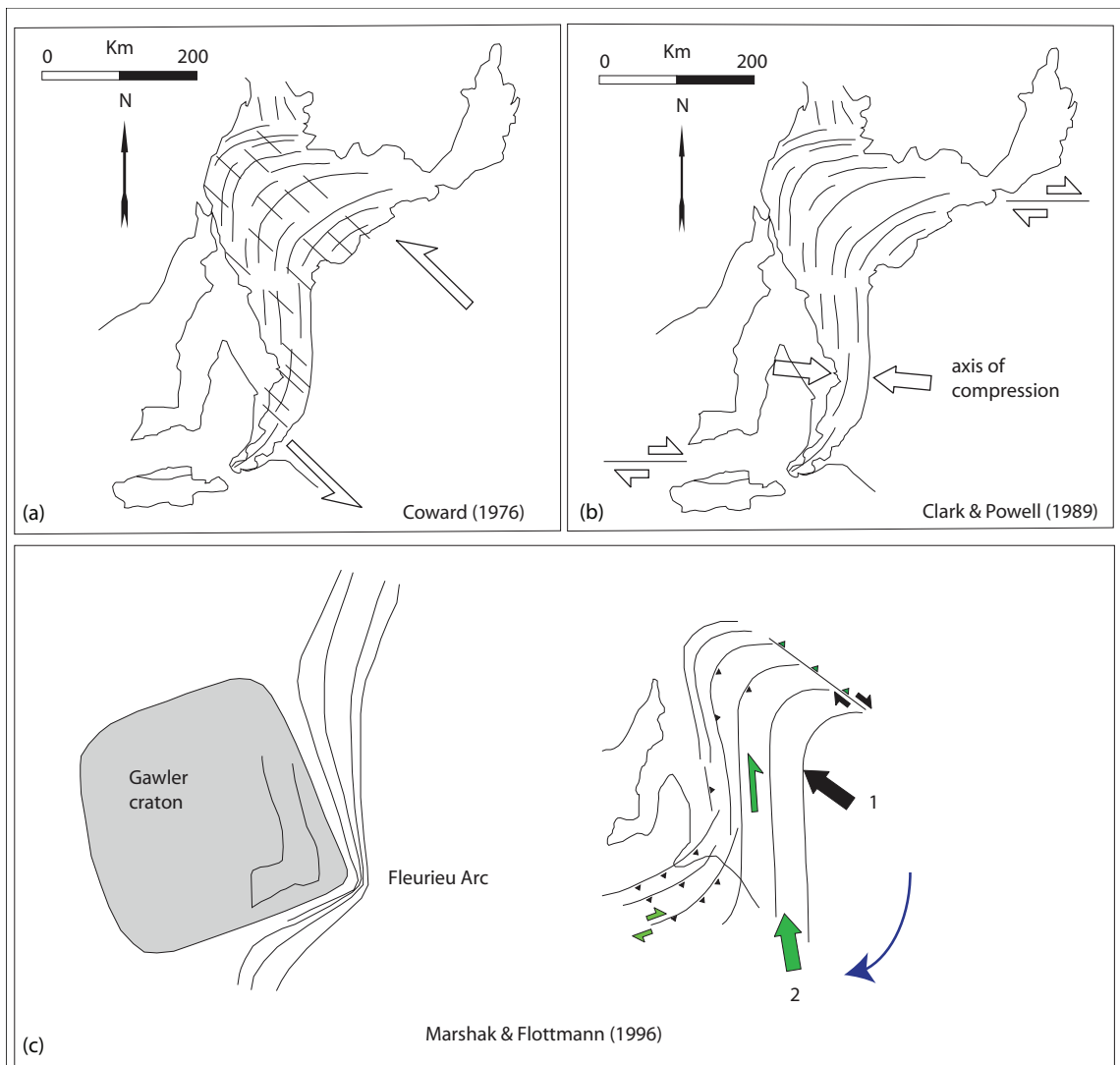


**Figure 1:** Figure modified from Marshak & Flöttman (1996) showing the three different orocline development geodynamic models for the Adelaide Geosyncline S-shape. In (a) the author propose that the convergence is oblique to the orocline trend, in (b) asymmetric synthesis are suggested and in (c) the oroclinal shape is explained by the impingement on the south-eastern corner of the Gawler Craton and a progressive clockwise rotation of the regional shortening direction (from 1 to 2).

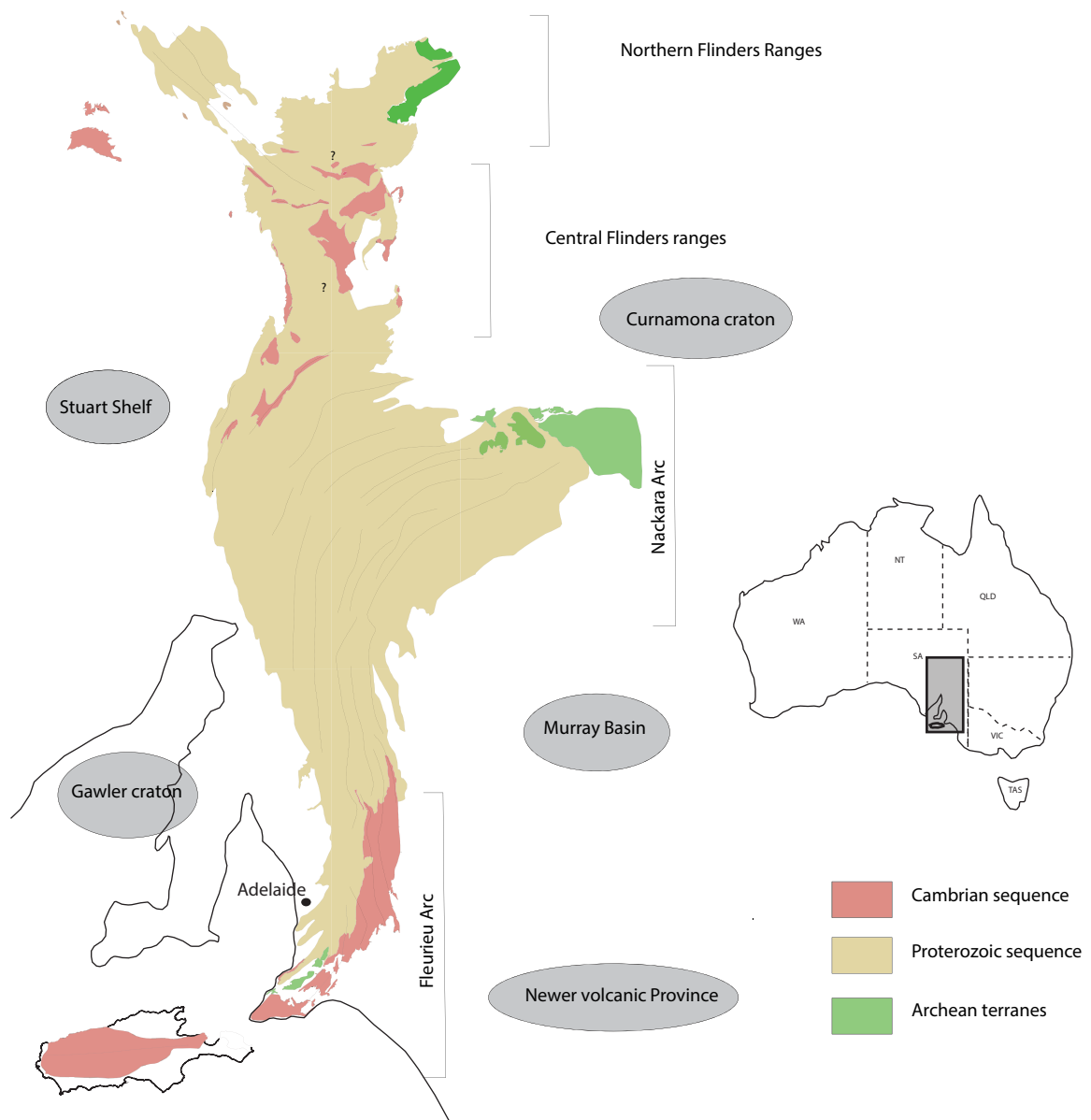


**Figure 2:** Regional structural map of the Adelaide geosynclines. This figure shows the main regional structural unit Nackara arc, Fleurieu arc, Central flinders, Northern Flinders, Gawler craton, Curnamona craton, Stuart shelf. The thin black lines correspond to the general tendency of regional fold axial plane traces.

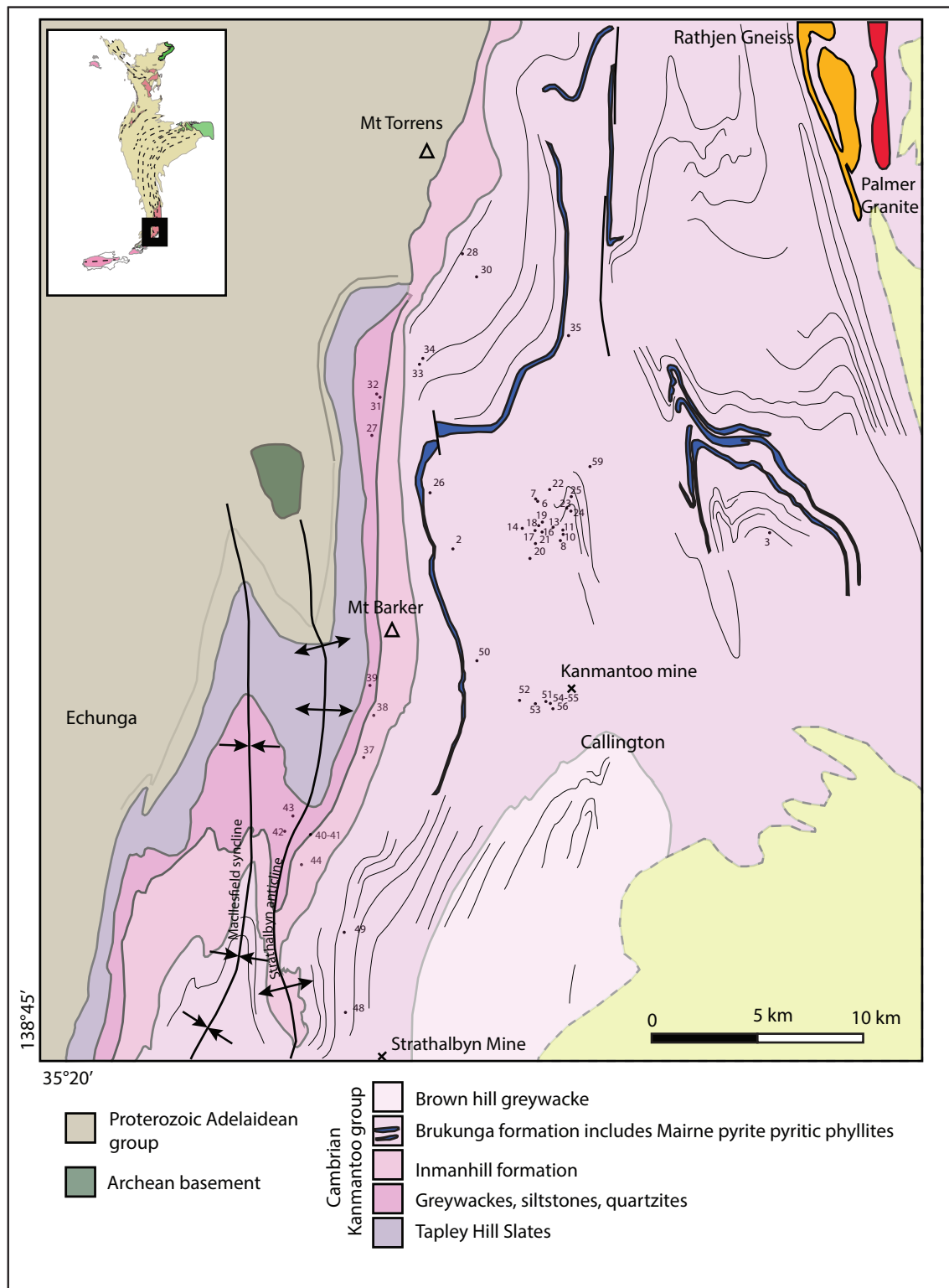


**Figure 3:** Structural map of the southern Mount Lofty range, with main structural elements, lithology and samples location.

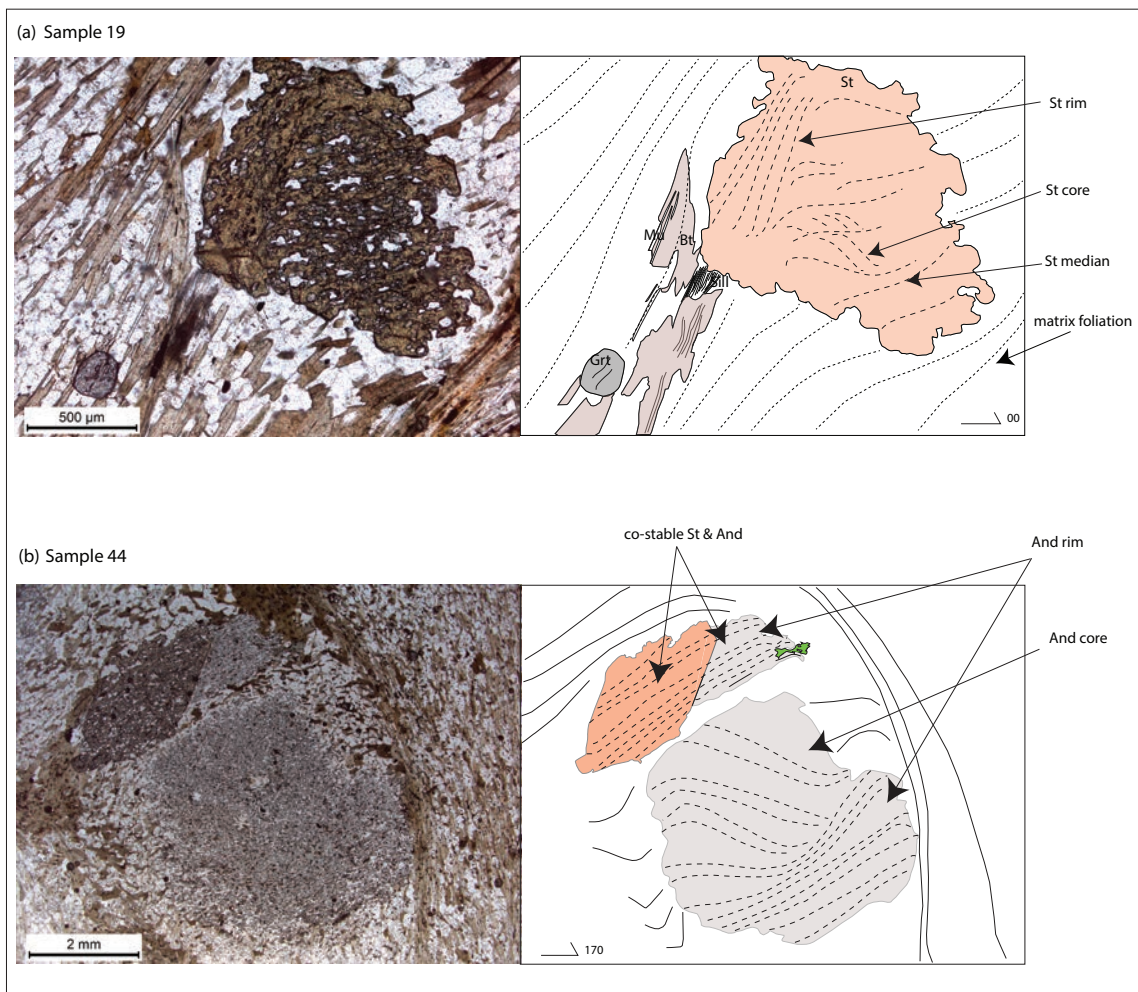


**Figure 4:**

(a) Photomicrograph and line diagram of a staurolite porphyroblast with trails defining a core, median and rim. Plane polarized light.

(b) Photomicrograph and line diagram of texturally stable staurolite and andalusite porphyroblasts with, trails continuous from one to the other and a larger andalusite with trails defining a core and rim. Note the extreme partitioning of high strain on the right side of the andalusite that truncates the trails in its right rim. Plane polarized light.

The porphyroblast core & rim terminology refers both to microstructures (a) and textures (b).

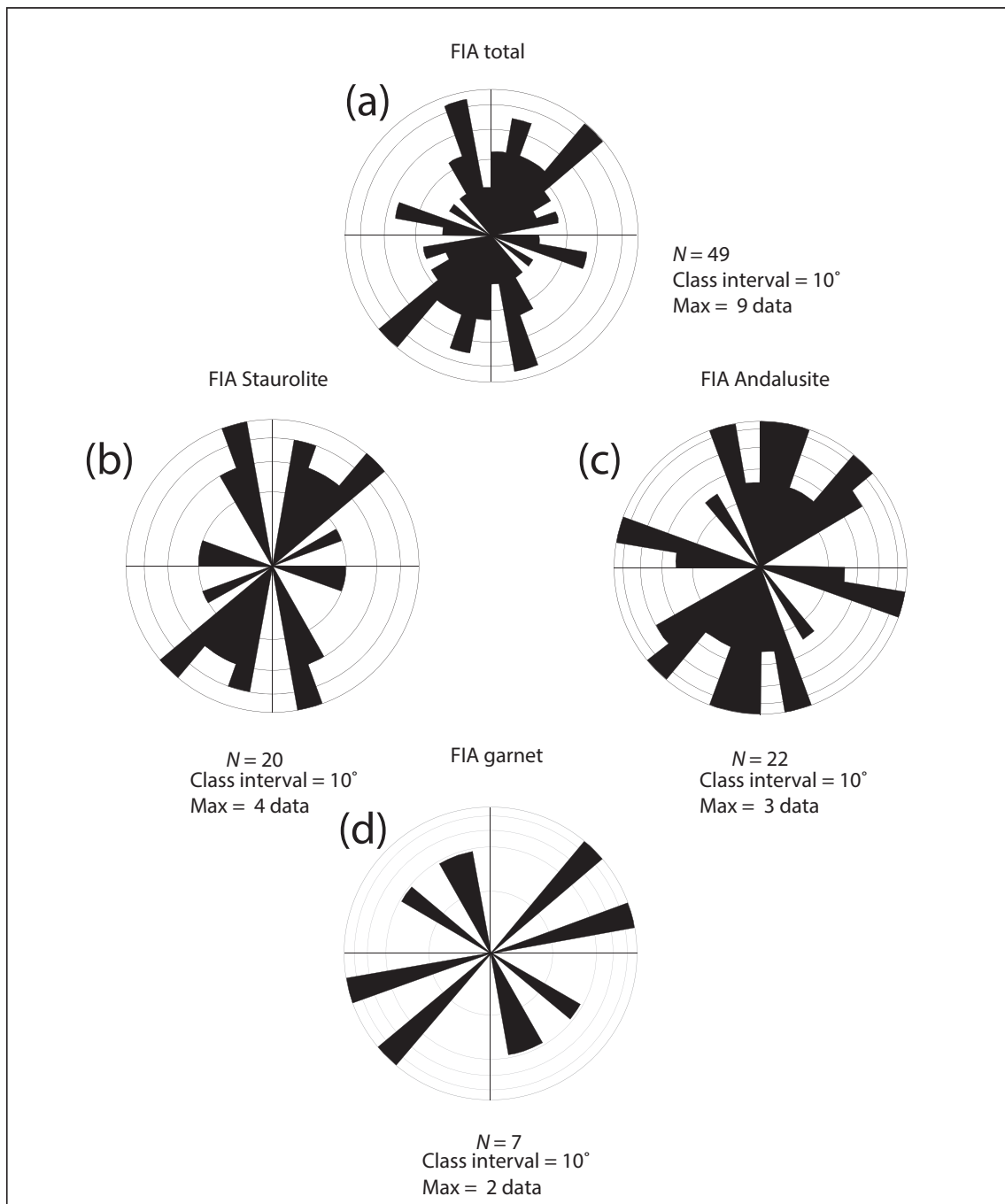


**Figure 5:** Rose diagrams (equal area) of FIAs for all porphyroblasts (a), for staurolite (b), for andalusite (c) and for garnet (d).

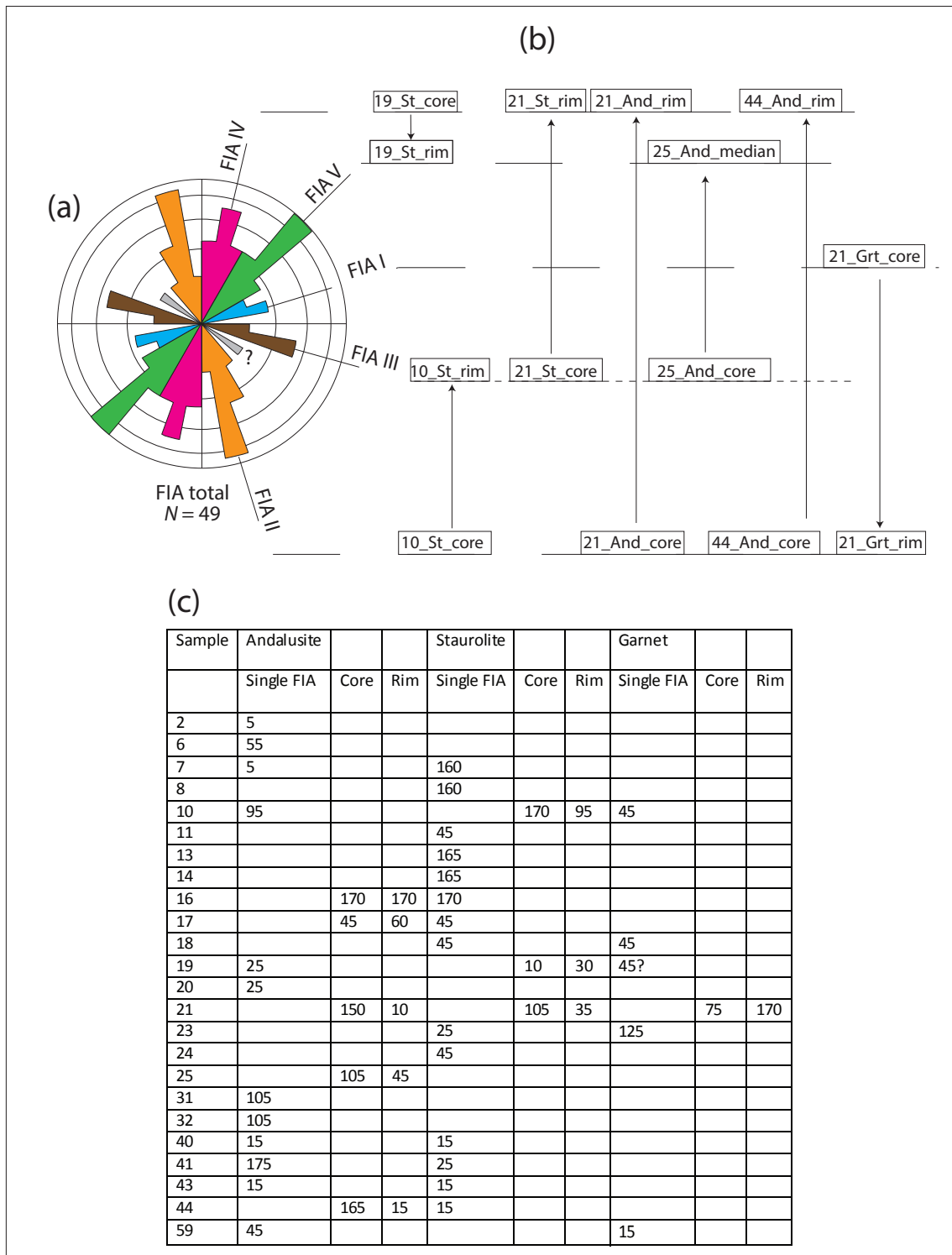
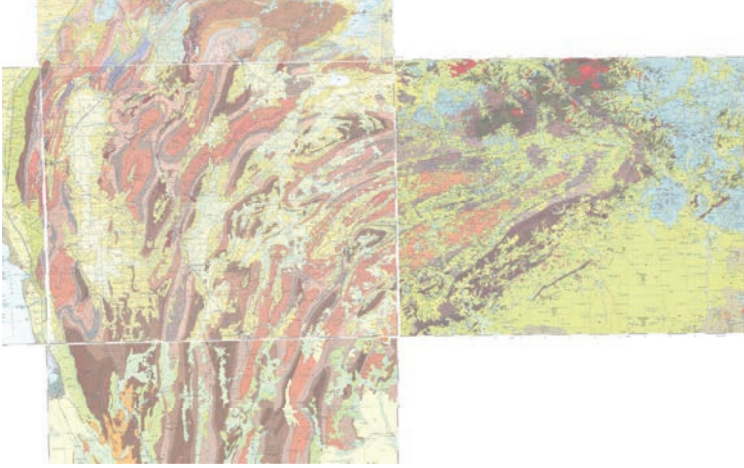
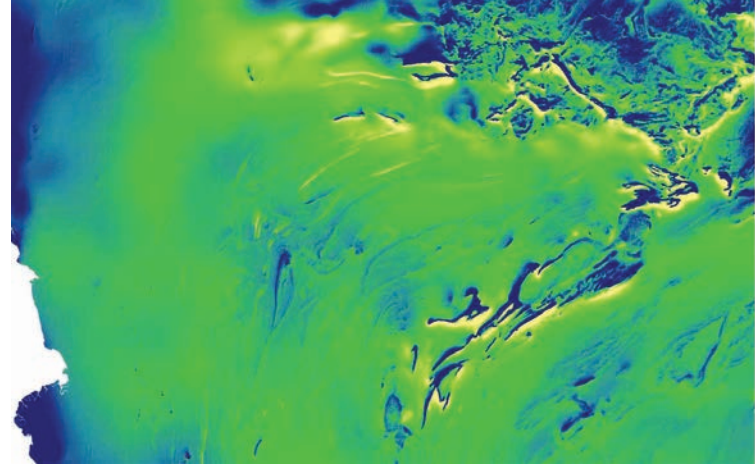


**Figure 6:** Equal area rose diagram for all FIAs in (a). (b) shows the relative timing of FIA based on core to rim relationship and (c) is a table of all FIAs measured showing their trend, mineral host, location within host and FIA set from the succession shown in (b). In sample 17 the FIAs measured in andalusites cores and rims are only 15° apart and most probably represent a single anastomosing FIA set. However for sample 19, despite having a staurolite core FIA and staurolite rim FIA measured a 20° from one another, they correspond of two individual FIA sets. It is that these trends pitch on two different top hats distribution, therefore they are to be statistically individualised.

(a)



(b)



(c)



(d)

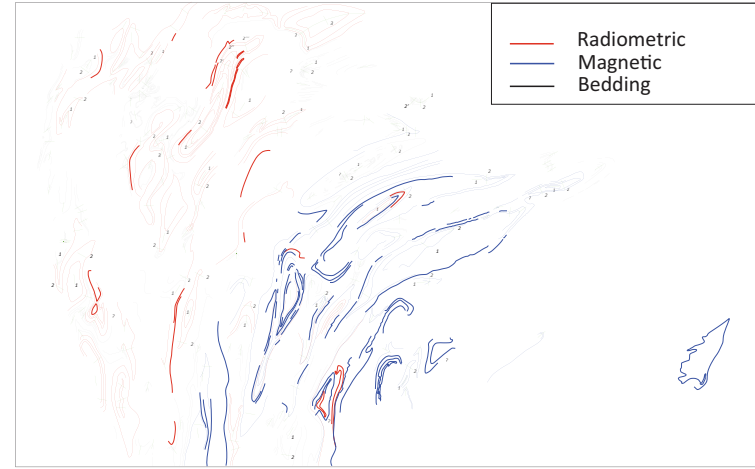


**Figure 7:** shows all the available maps for the Nackara arc; Compilation of 1/250000 geological maps (a) and geophysical i.e aeromagnetic (b) and radiometric (c). (d) shows the detailed bedding geometry inferred from (a), (b), (c).

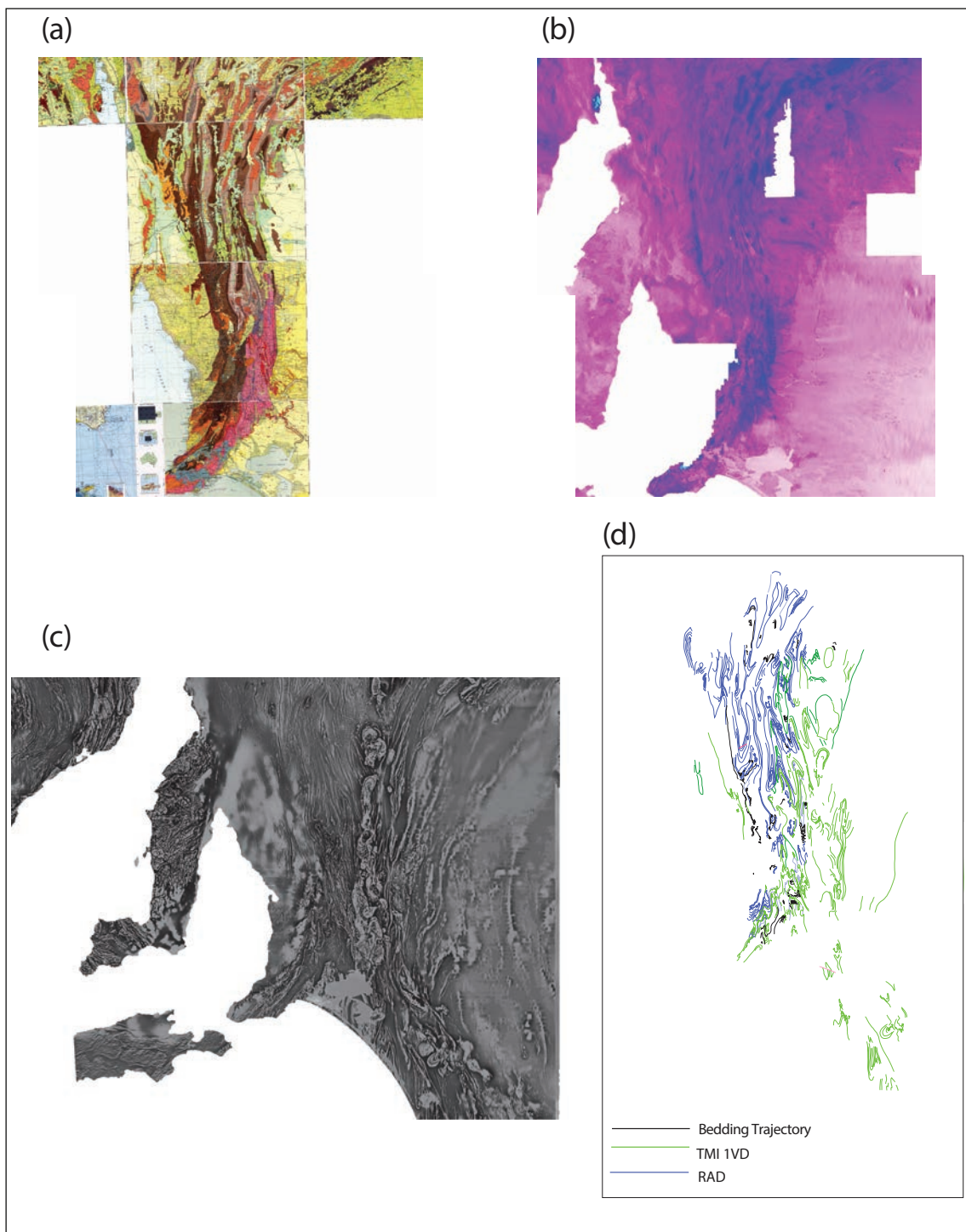


**Figure 8:** shows all the available maps for the Fleurieu arc; Compilation of 1/250000 geological maps (a) and geophysical i.e. radiometric (b) and aeromagnetic (c). (d) shows the detailed bedding geometry inferred from (a), (b), (c).

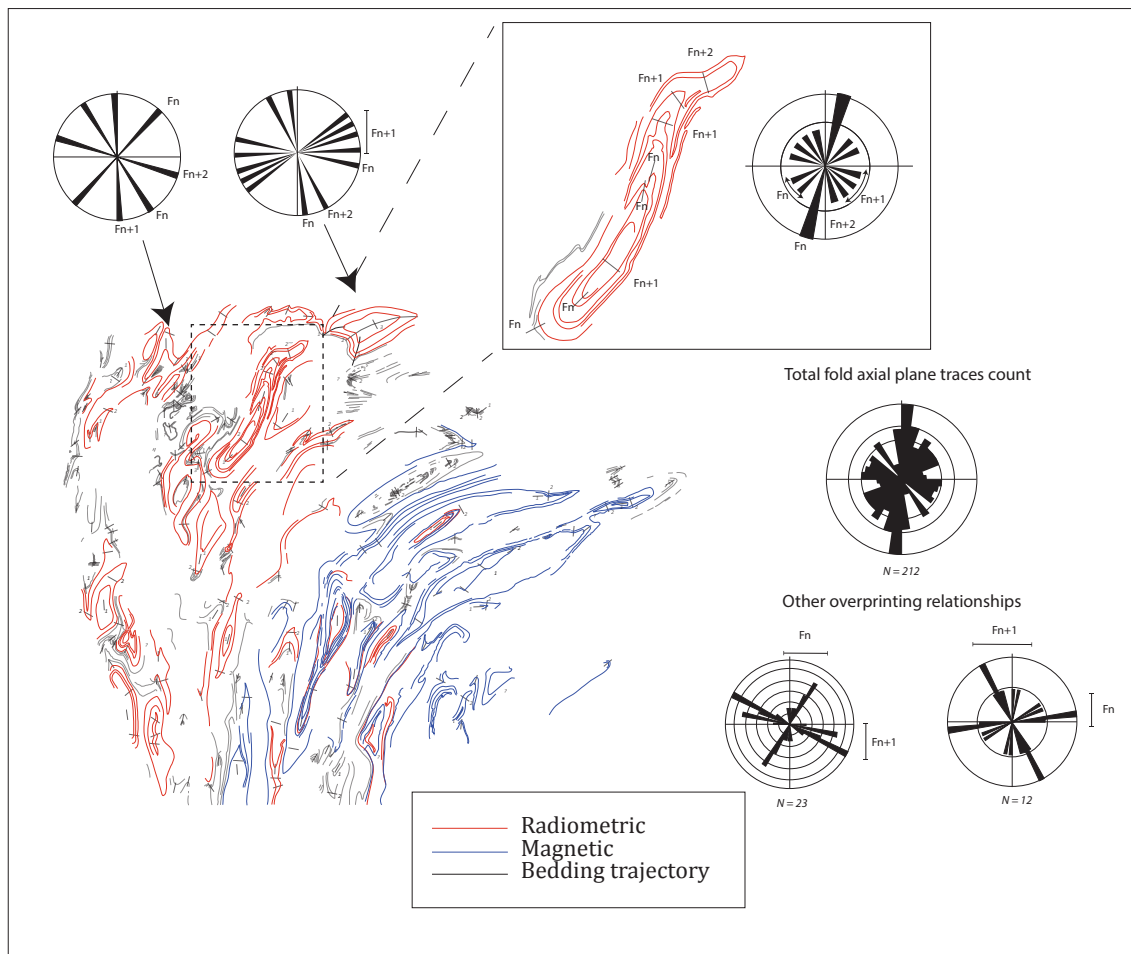


**Figure 9:** Map showing axial plane trends measured from the combined bedding interpretative map of the Nackara arc from Fig. 7d. Total axial planar axis and significant fold overprinting relationships are also plotted on rose diagram in this map.

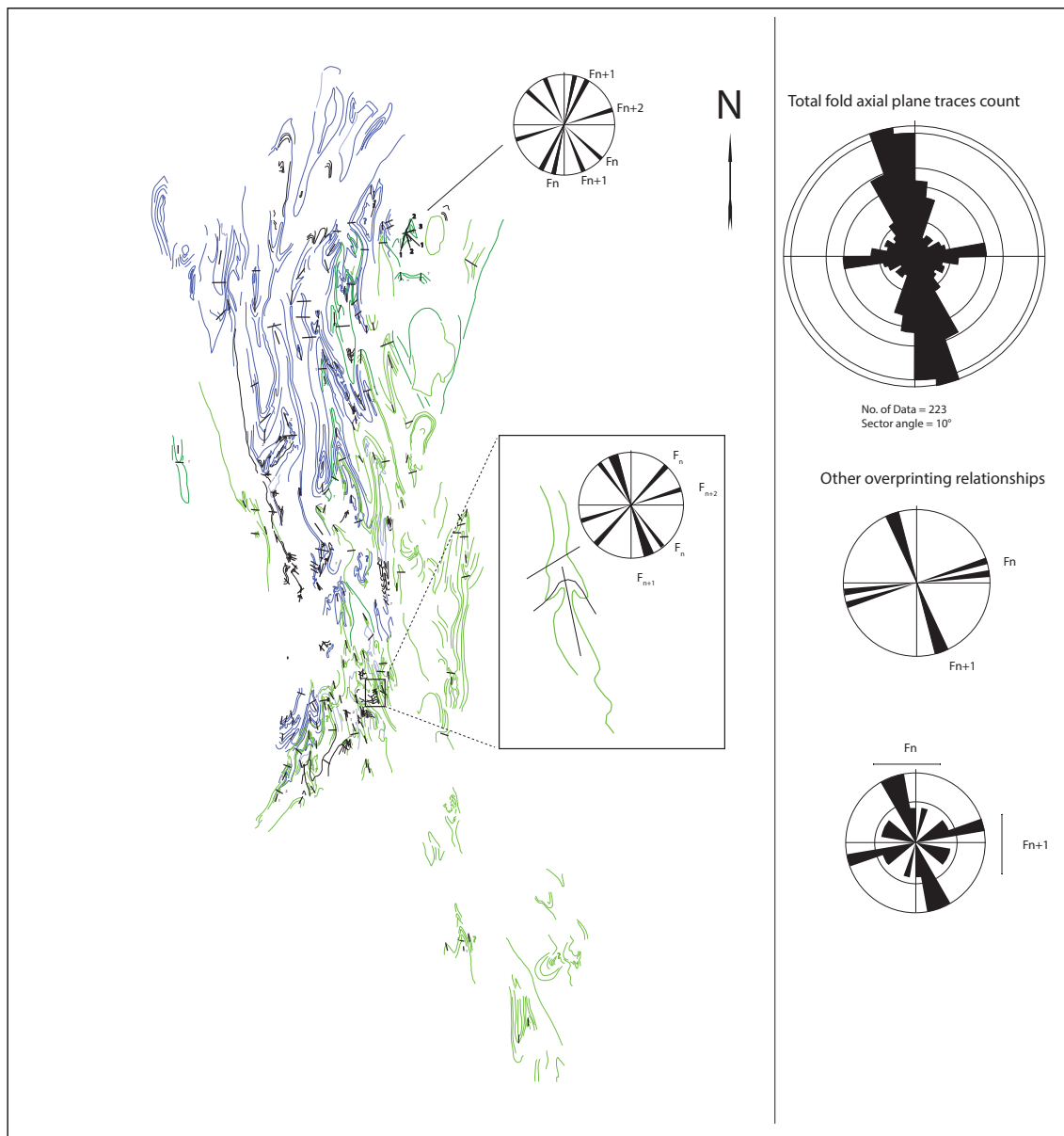


**Figure 10:** Map showing axial plane trends measured from the combined bedding interpretative map of the Fleurieu arc from Fig. 8d. Total axial planar axis and significant fold overprinting relationships are also plotted on rose diagram in this map.

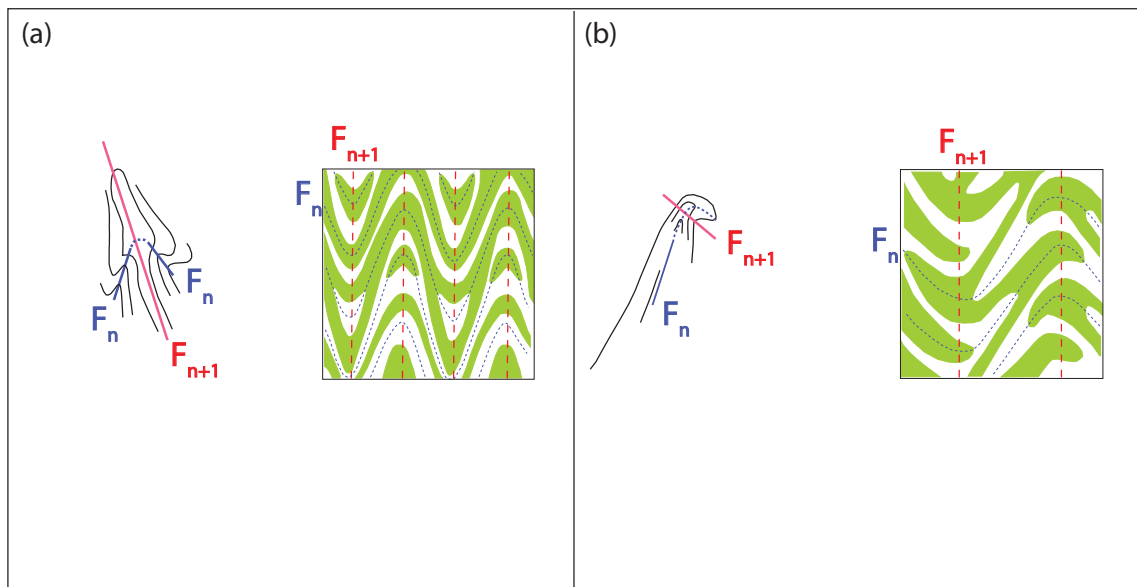
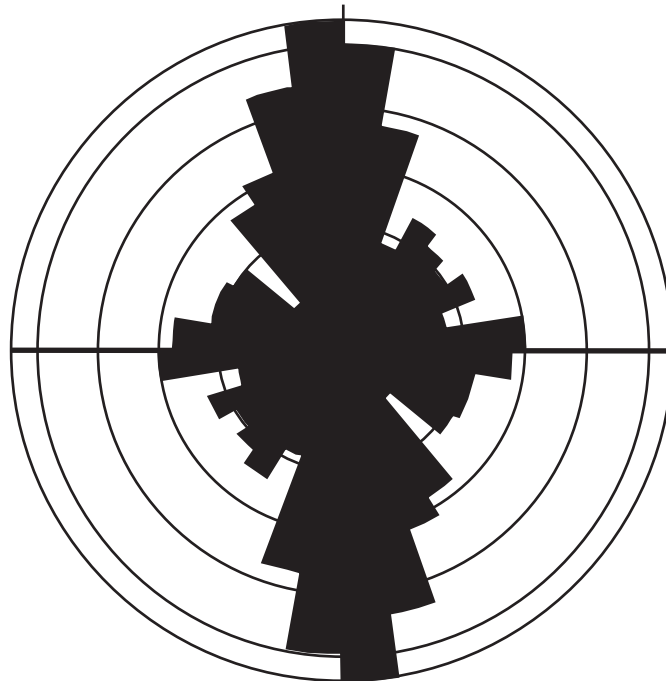


**Figure 11:** (a), (b) show examples of refolding structures: theoretical on the LHS, from Thiessen & Means (1980); interpreted from the analysis of the combine geophysical and geological dataset on the RHS.

Combine Fold axial planes traces  
for bottom and middle zone



No. of Data = 435  
Sector angle = 10°  
Max = 47

**Figure 12:** Plot on a rose diagram of the compilation of all fold axial planar axis for the Fleurieu and Nackara arc.

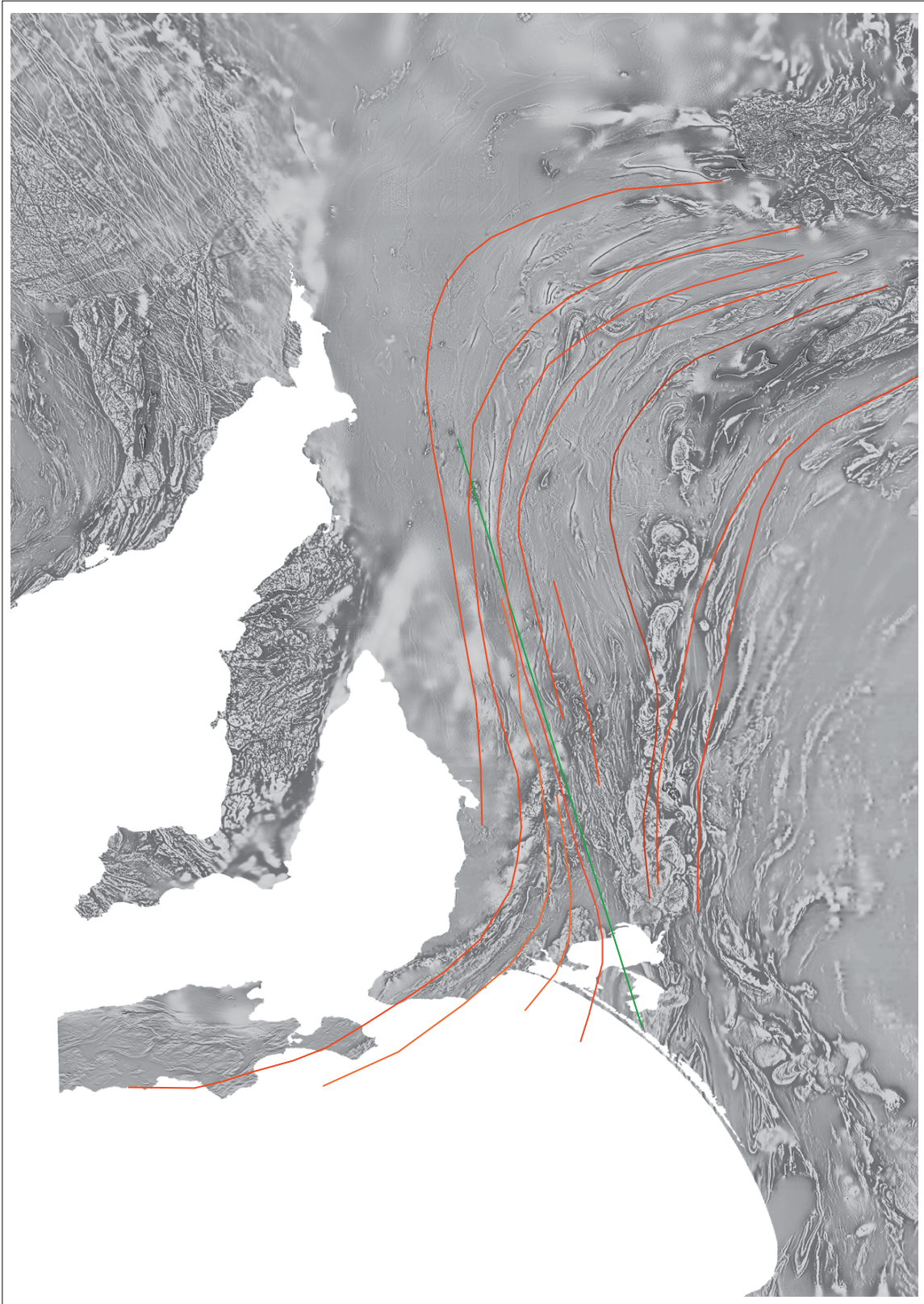


**Figure 13:** Aeromagnetic Map (first derivative of the magnetic intensity) of the Adelaide geosyncline showing an  $\sim 345^\circ$  trending zone of high shear strain rotates the W-E trends to the east of the Nackara Arc to more N-S trends and is more intensely developed and even truncational where it rotates the W-E trends of Kangaroo Island.

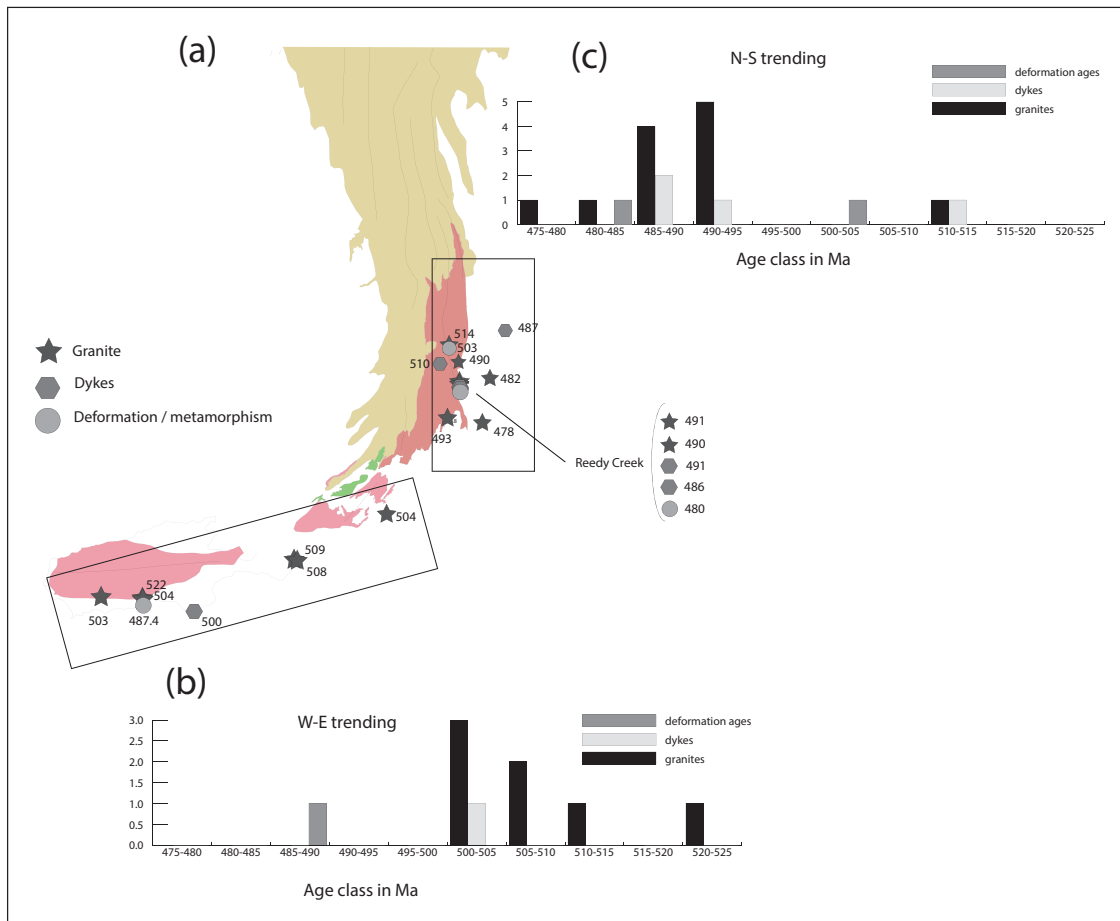


**Figure 14:** Shows the location of intrusives and metamorphic their ages compiled from the accessible literature. Different symbols for granite, gneiss and dykes in (a).

(b) is the Histograms of the intrusive ages for the W-E trending Kangaroo Island domain. (c) is the Histograms of the intrusive ages for the N-S trending zone in the mainland to the E of Kangaroo Island.

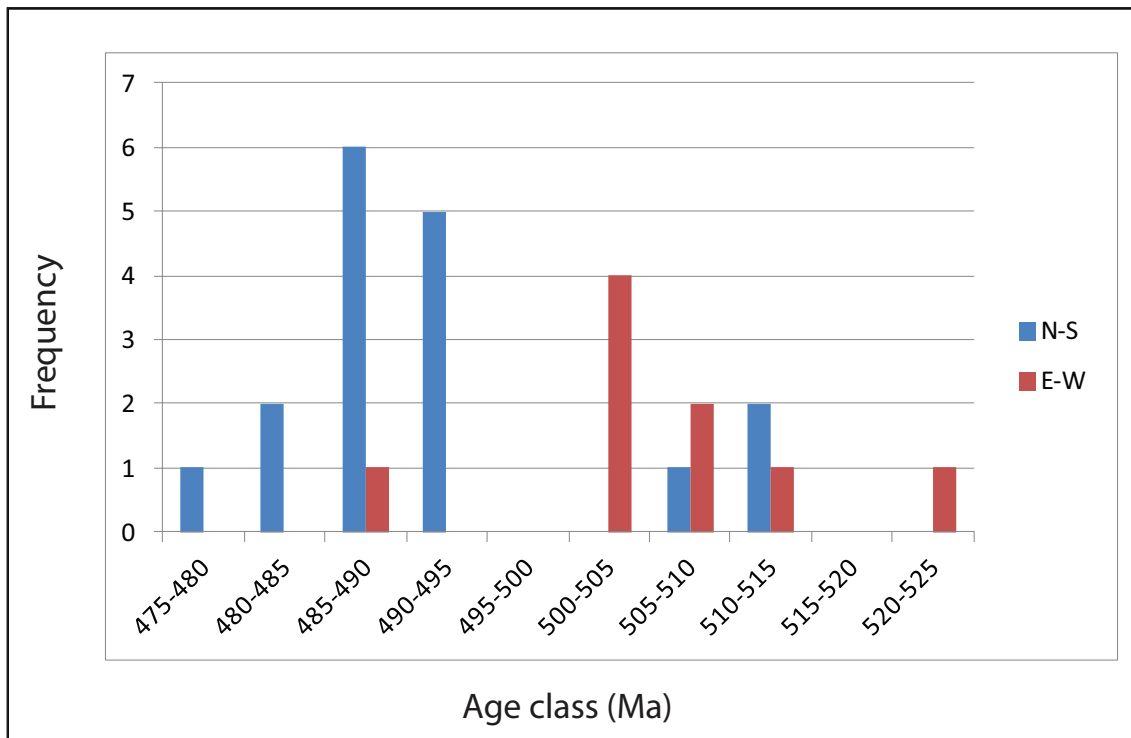


**Figure 15:** Composite histogram of West-East and North-South Delamerian ages from Kangaroo Island the southern delimitation of the Nackara Arc

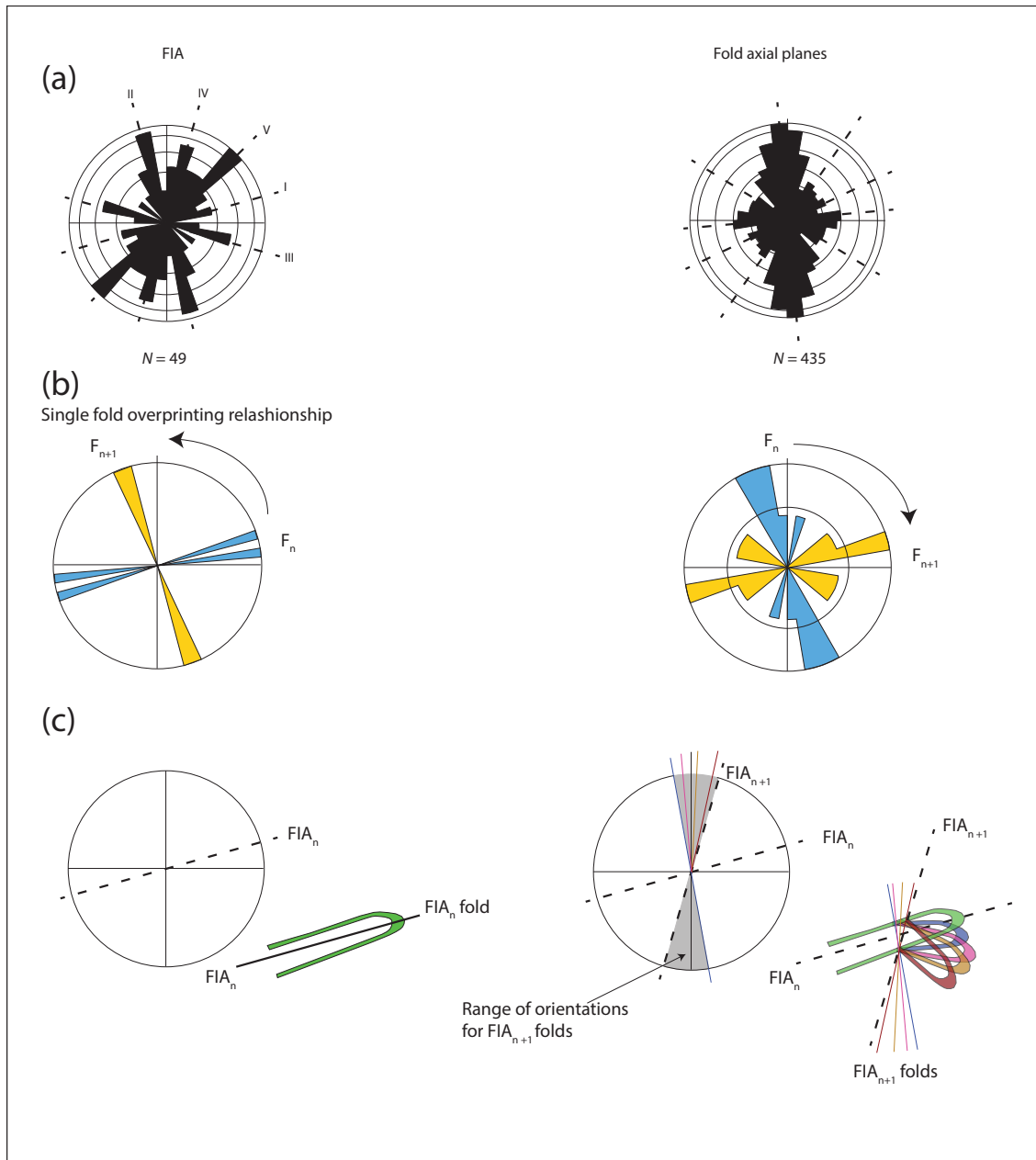


**Figure 16:** Comparison of the peaks in distribution of fold axial plane traces & FIAs.

(a) Equal area rose diagram showing the orientation of FIAs on the LHS. Equal area rose diagram showing the orientation of the fold axial planes on the RHS. (b) Rose diagrams of single overprinting relationships between two successive fold generations that follows the shift in bulk shortening direction unravelled by the FIA successions. FIA I to FIA II for the RHS fold interference rose diagram and FIA II to FIA III for the LHS fold interference rose diagram. (c) Shows a theoretical illustration of the variability of fold axial planar cleavage traces produced by a single overprinting event due to the inhomogeneous rotation of fold limbs. The variable rotation of fold limbs from one FIA events to another explains the range of  $F_n$  and  $F_{n+1}$  orientation on the RHS of (b) and plays a role in the relative misfit between peaks in FIAs and the bulk of the Adelaide geosyncline fold axis in (a).

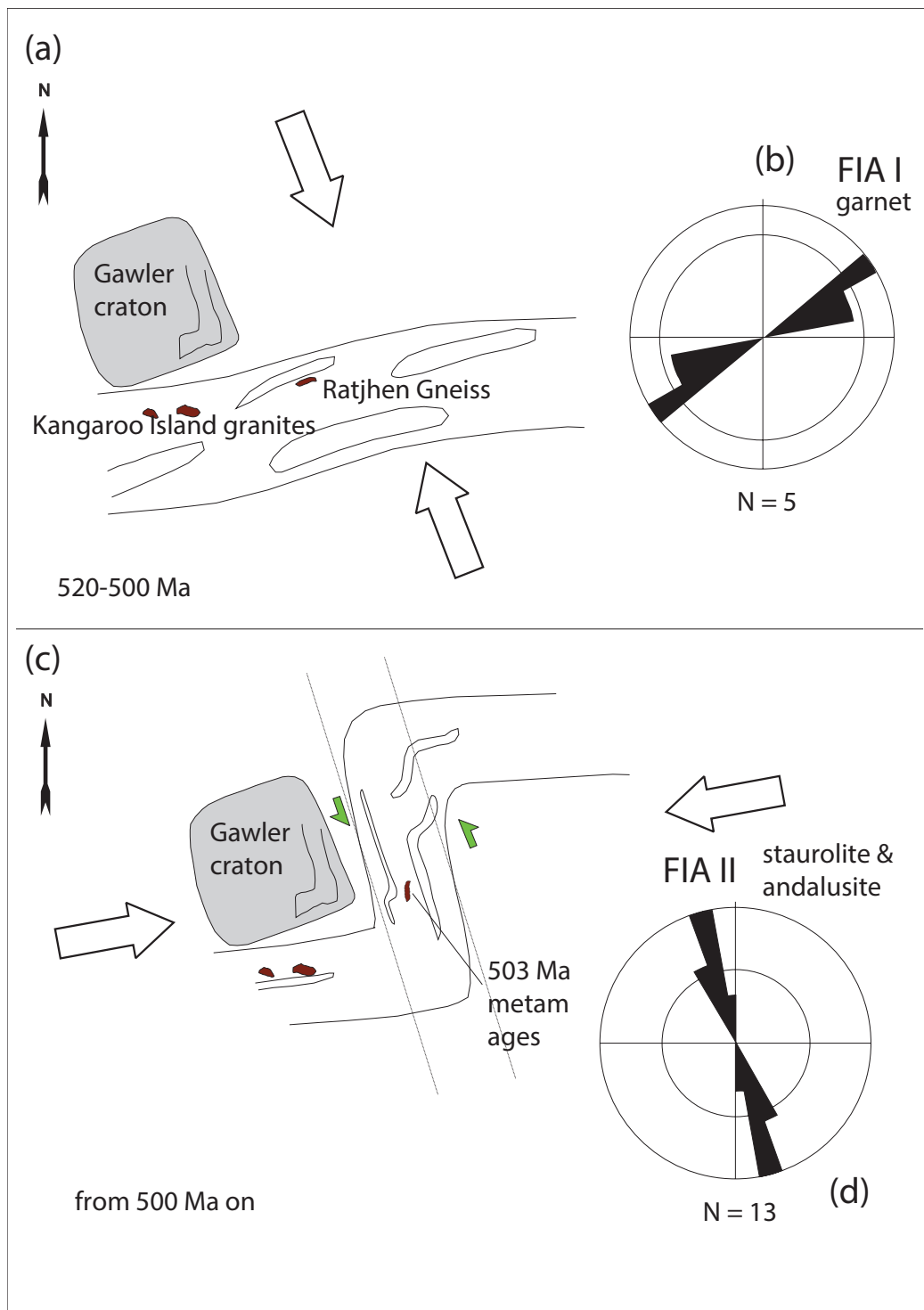


**Figure 17:** New geodynamic interpretation to the arcuate shape of Adelaide geosyncline. (a) shows ~E-W fold belt trend resulting from ~N-S bulk compression during FIA I (b). (c) ~W-E shortening has rotated a (median) portion of the belt into a N-S trend during FIA II (d).

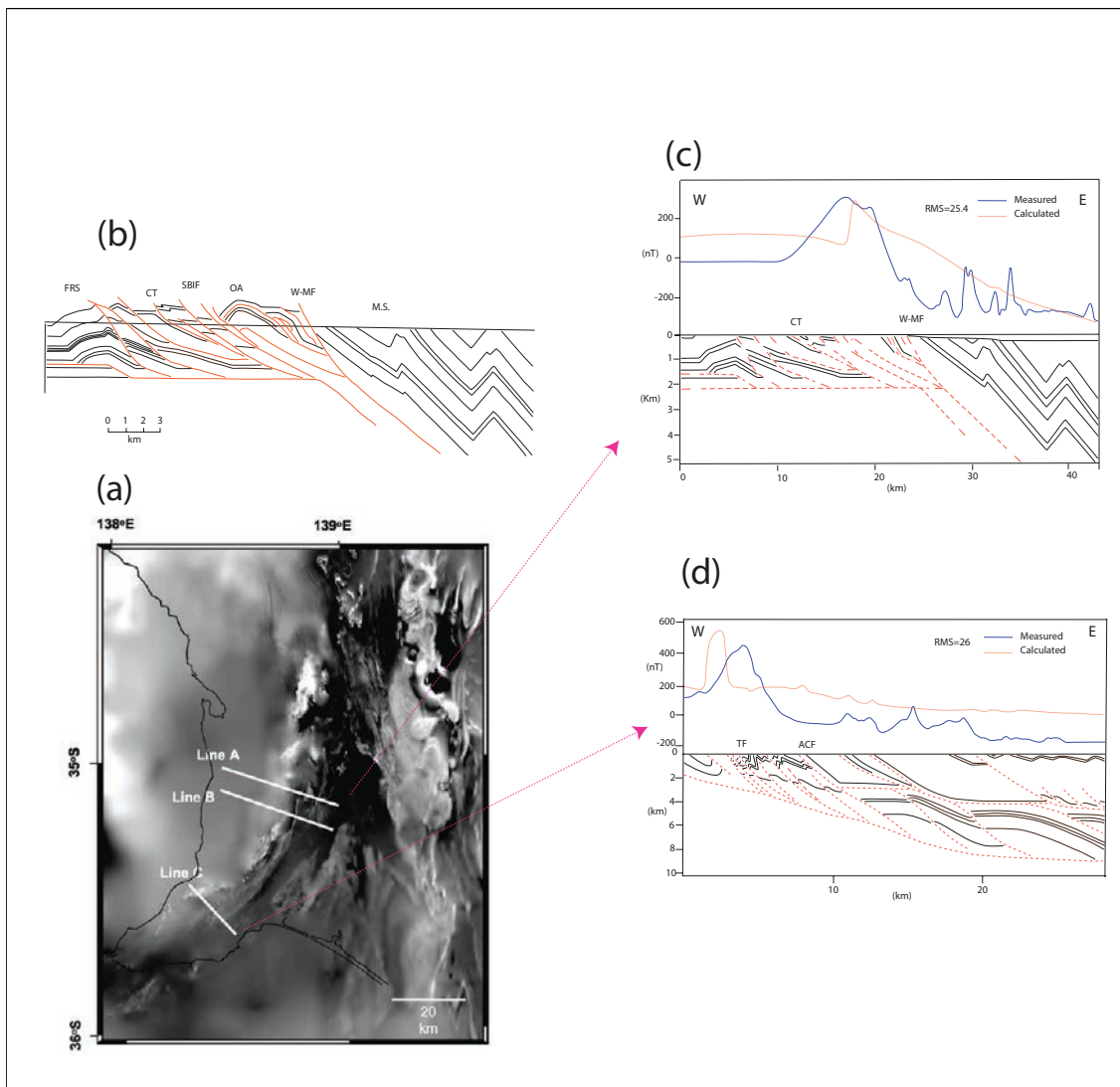


**Figure 18:** Figure modified from Direen et al. (2005) with on (a) cross section locations on the Fleurieu Arc TMI map. (b) is Flöttman et al. (1994) cross-section that propose major thrusting of the Kanmantoo to the West onto the Adelaidean. (c) and (d) are Direen et al. (2005) forward modeling cross section with calculated effect and measured anomaly.

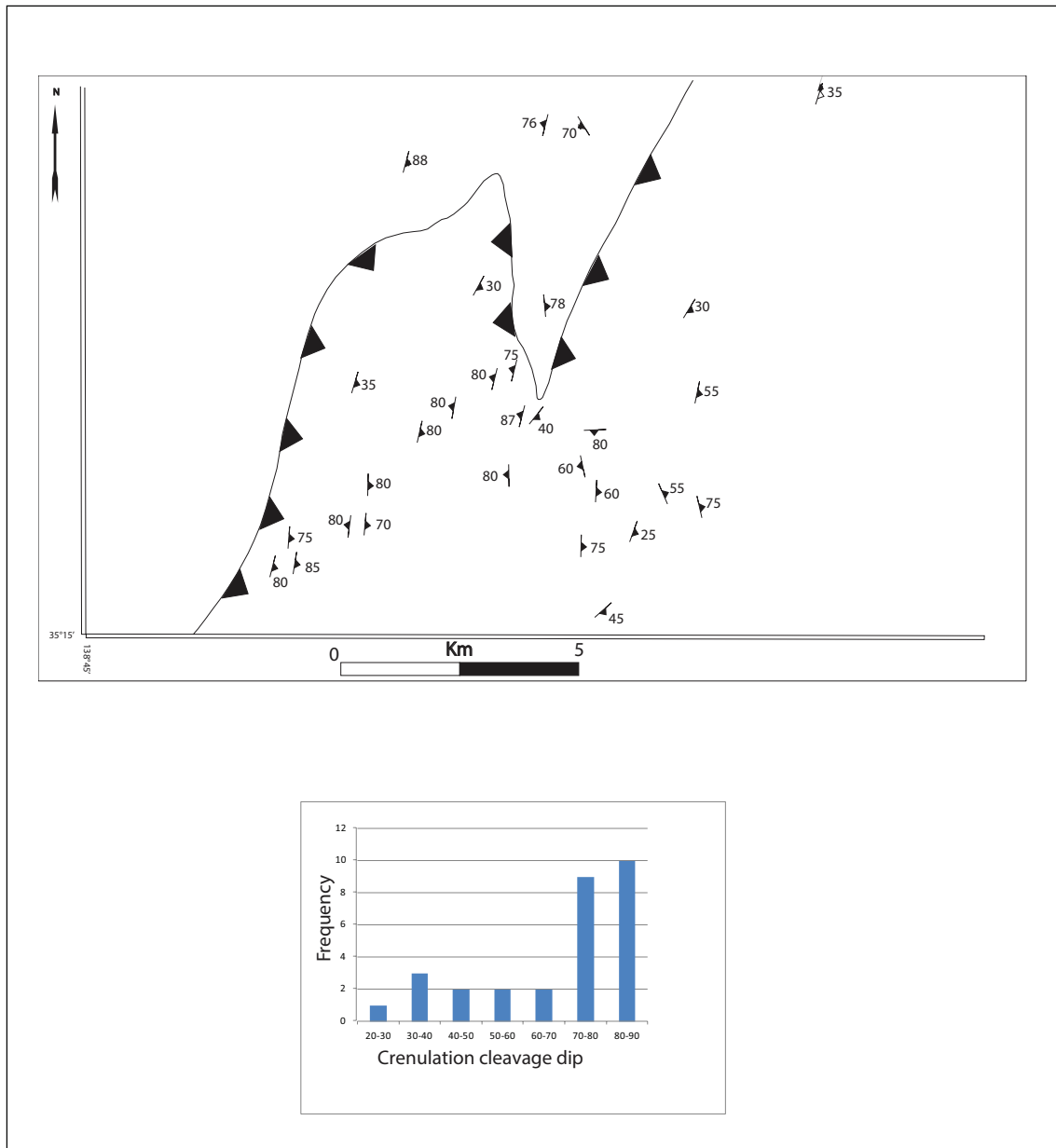


**Figure 19:** Simplified map and histogram of crenulation cleavages strike and dips in the Southern Mount lofty ranges at the proximity of the inferred thrust.

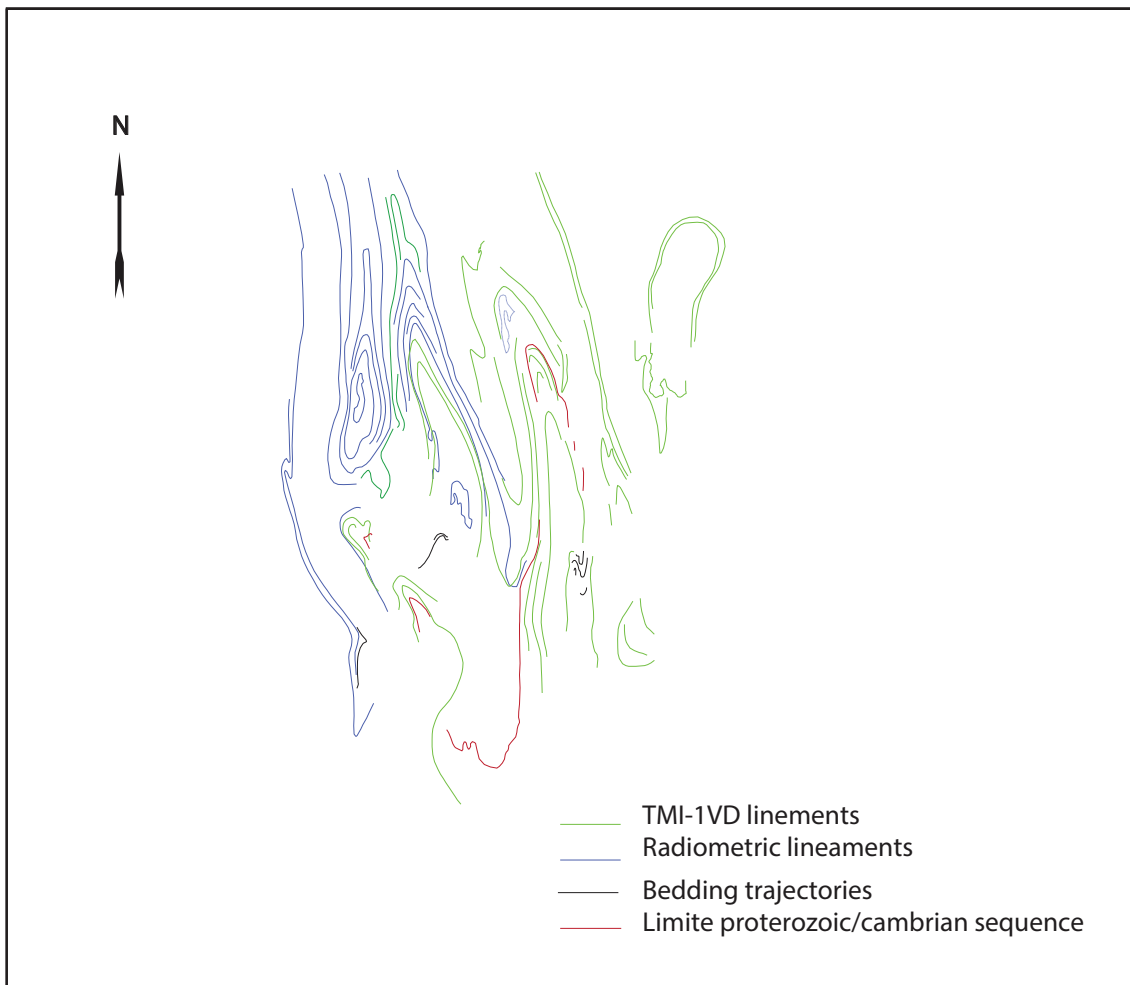


**Figure 20:** Enlargement of Fig. 10 focused on the major folds on both sides of the Kanmantoo-Adelaidean sediments contact showing their consistency across this boundary.

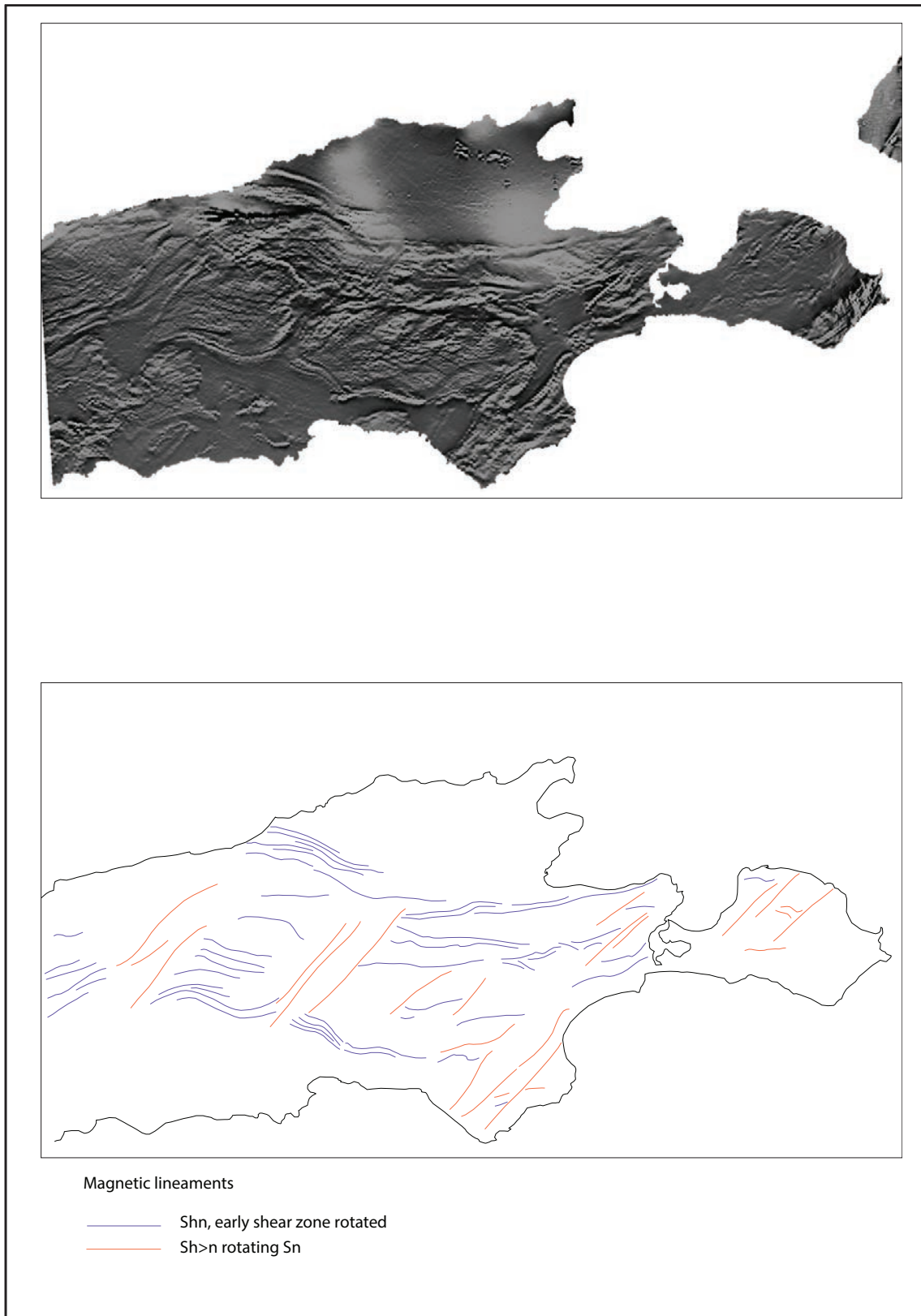


**Figure 21:** Aeromagnetic map (first derivative of the magnetic intensity) of Kangaroo Island structures. Total magnetic intensity image, first derivative – source GSA.

**- CHAPTER III-**

**INCLUSION TRAIL ANALYSIS TECHNIQUES, MULTIPLY  
INTERLEAVED GROWTH OF STAUROLITE AND ANDALUSITE,  
AND SHIFTING PARTITIONING OF REACTIONS VS  
DEFORMATION WITH TIME**

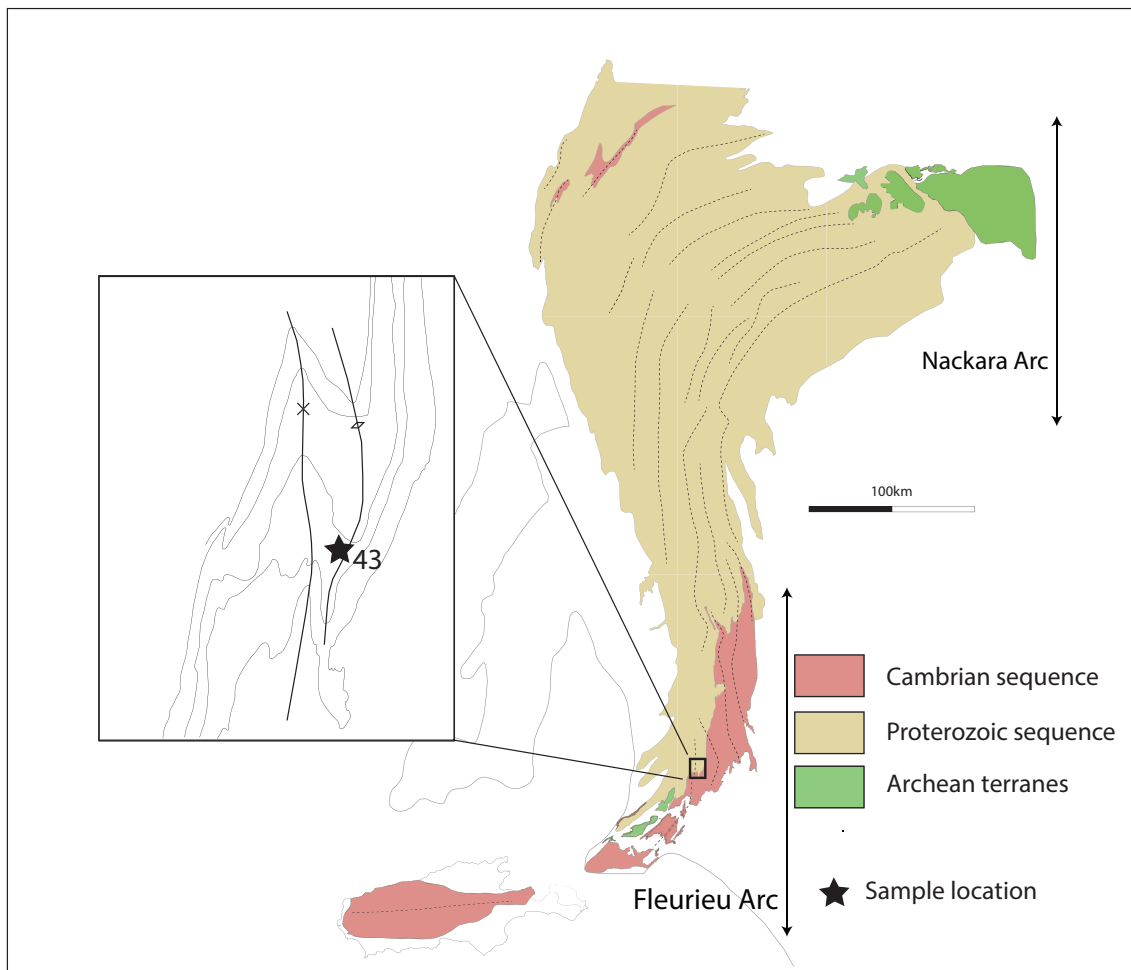


**Figure 1:**

Regional geology of Adelaide Fold Belt. The rectangular box expanded to the left shows the location of sample 43 relative to the Macclesfield syncline-Strathalbyn anticline fold couplet.

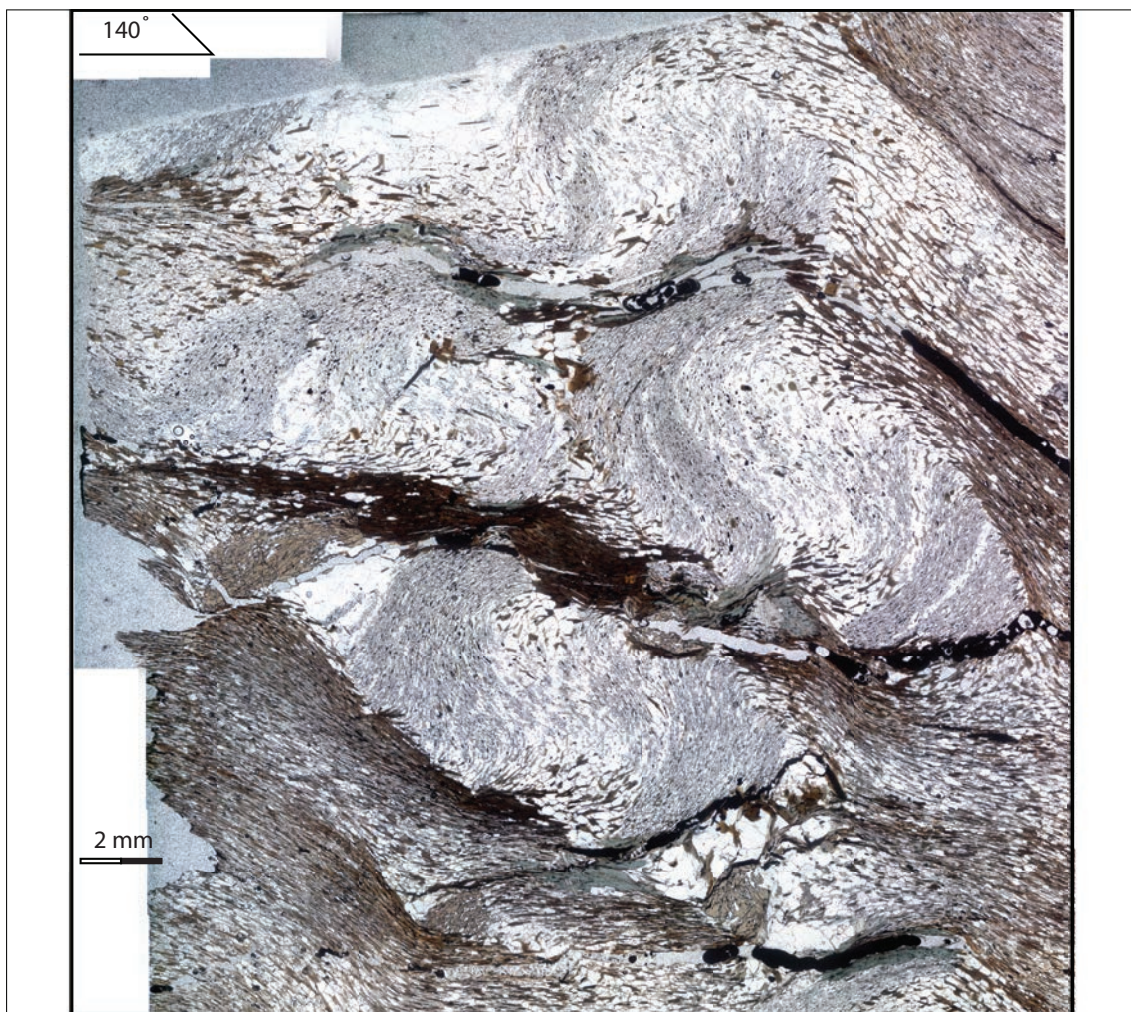


**Fig. 2a**

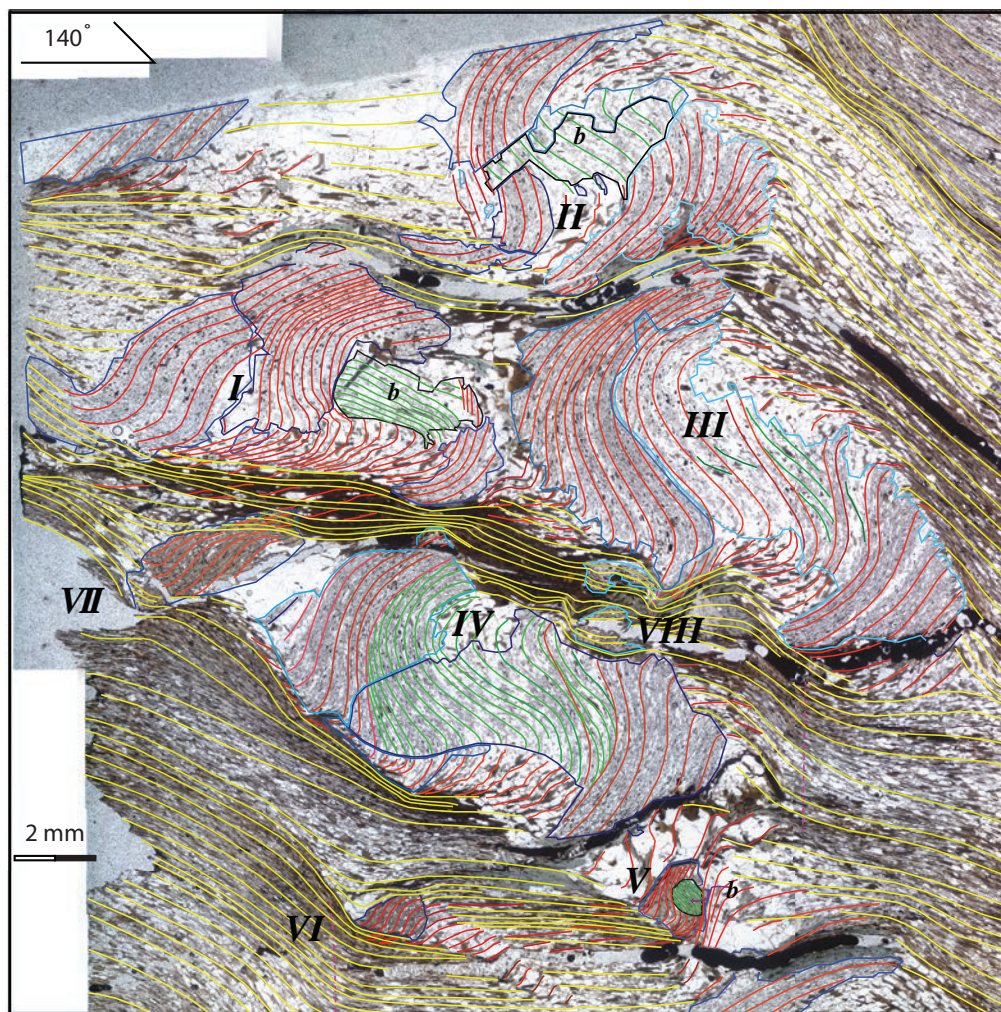


Fig. 2b

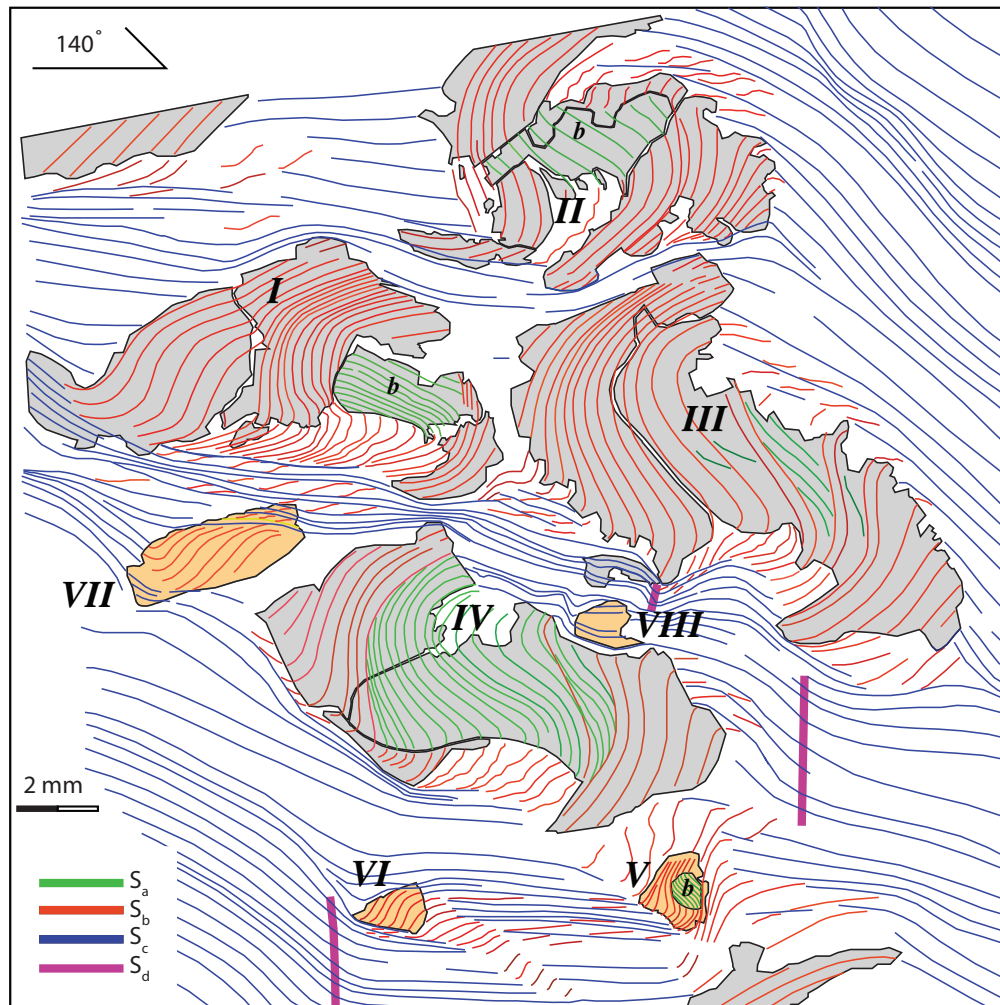


Fig. 2c

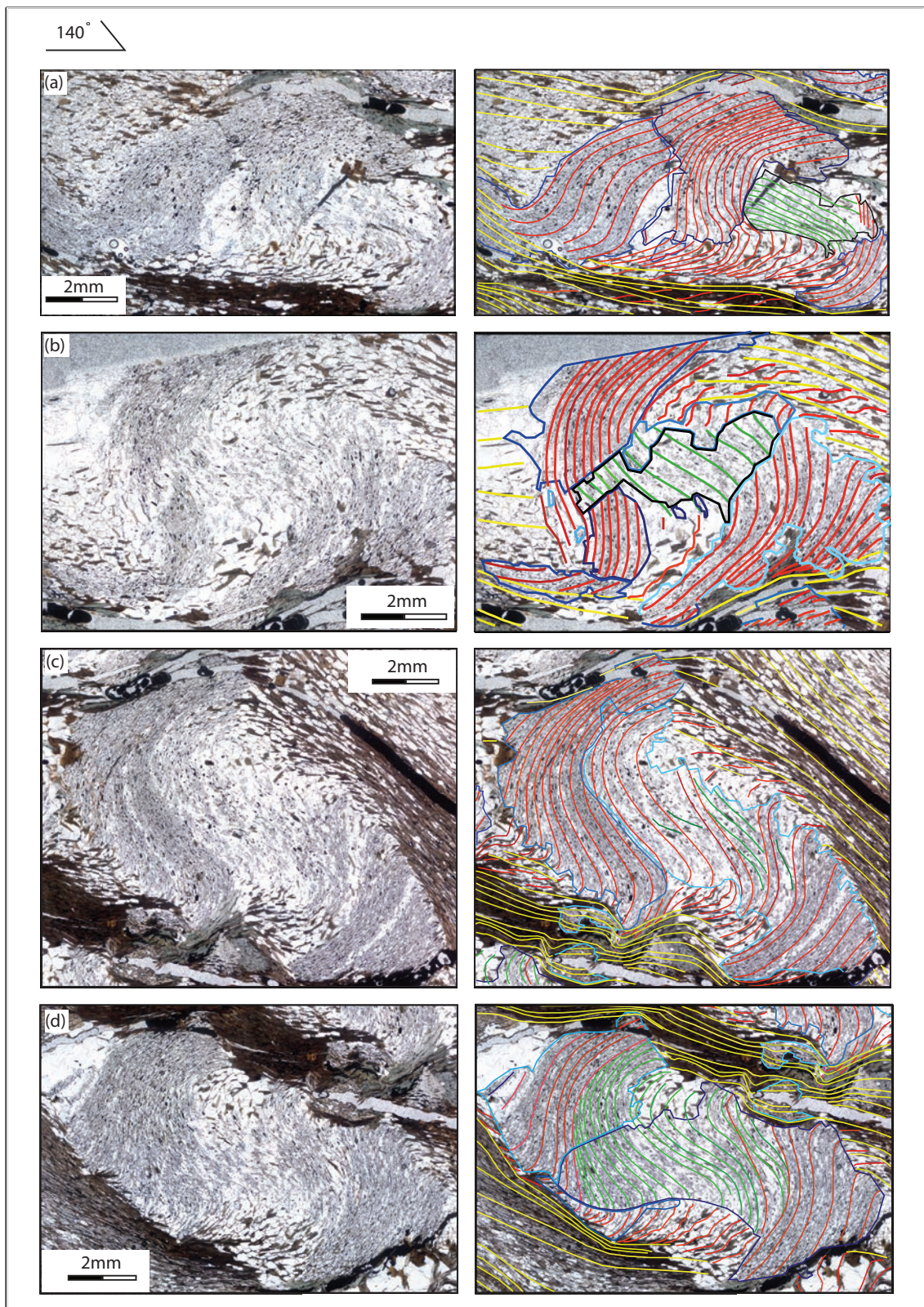
**Figure 2:**

Andalusite and staurolite porphyroblasts in a vertical thin section striking at  $140^\circ$

a) High resolution photo of much of the thin section.

b) Line diagram superimposed on (a) of foliations in the matrix, foliation preserved as inclusion trails and the boundaries of porphyroblasts, including differently oriented andalusite crystals with the clusters labelled *I*, *II*, *III* and *IV*. Microstructural cores in *I*, *II* and *V* are labelled “b” because as shown later, they grew early during the development of  $S_b$ .  $S_a$  is green,  $S_b$  is red and the trend of  $S_c$  axial planes is shown in purple in 2 locations. Porphyroblasts *V*, *VI*, *VII* and *VIII* are staurolite. The crenulation cleavage  $S_b$  is ranges from a differentiated crenulation cleavage at stage 3 of development (Bell & Rubenach, 1983) where the crenulated cleavage  $S_a$  is continuous with  $S_a$  to one at stage 4 where it truncational along zones of  $S_b$  differentiation. This is typical of the growth effects of porphyroblasts on truncational development (Bell & Hayward, 1991).

c) Same line diagram as (b) without the photomicrograph.  $S_c$  is here in blue.



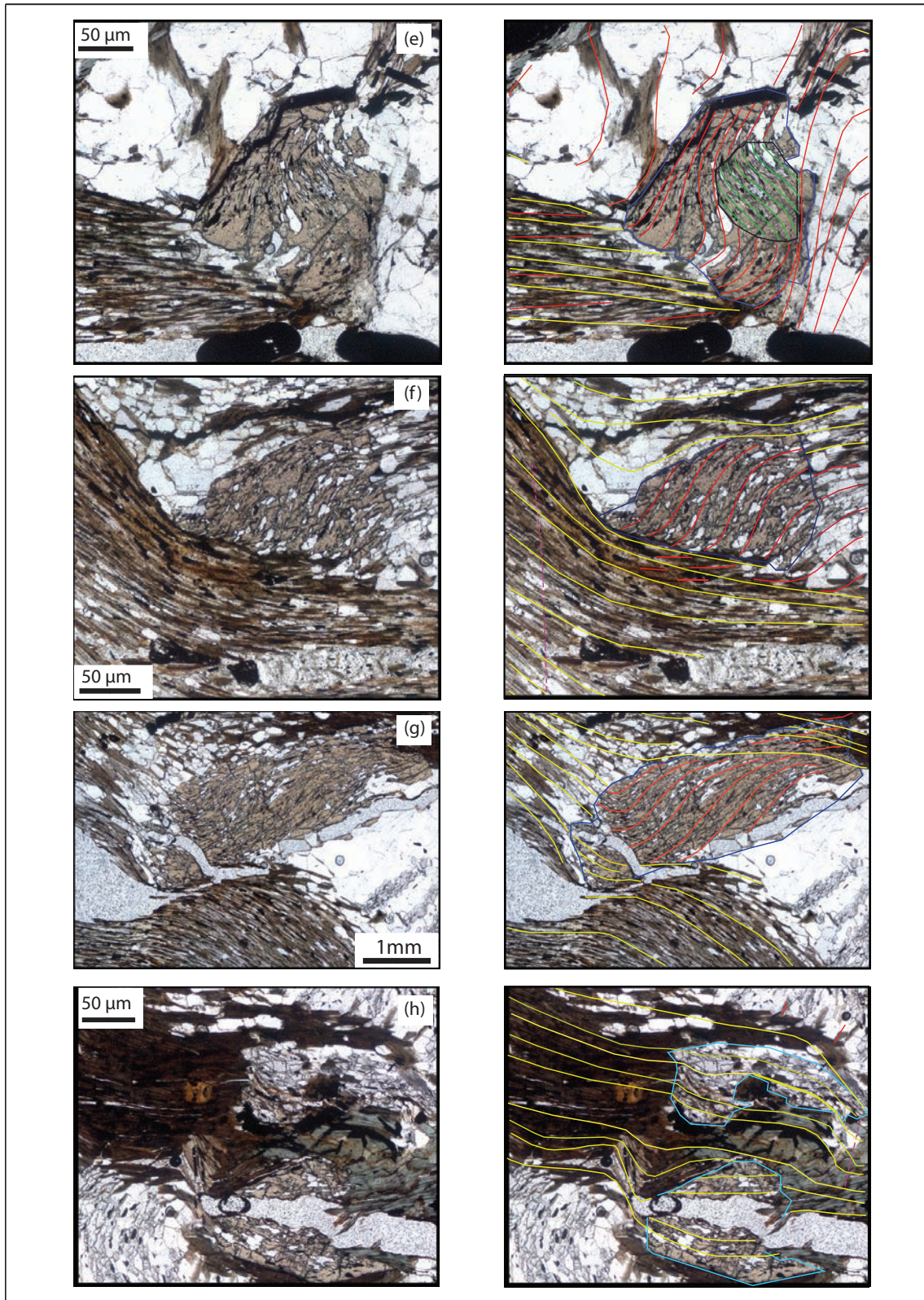


**Fig. 3e, f, g, h**

**Figure 3:** Magnified images from Fig. 2 of *I* (a), *II* (b), *V* (c), *III* (d), *IV* (e), *VI* (f), *VII* (g) and *VIII* (h) with inclusion trails overlaid over each photo down the right side. Described in the text.

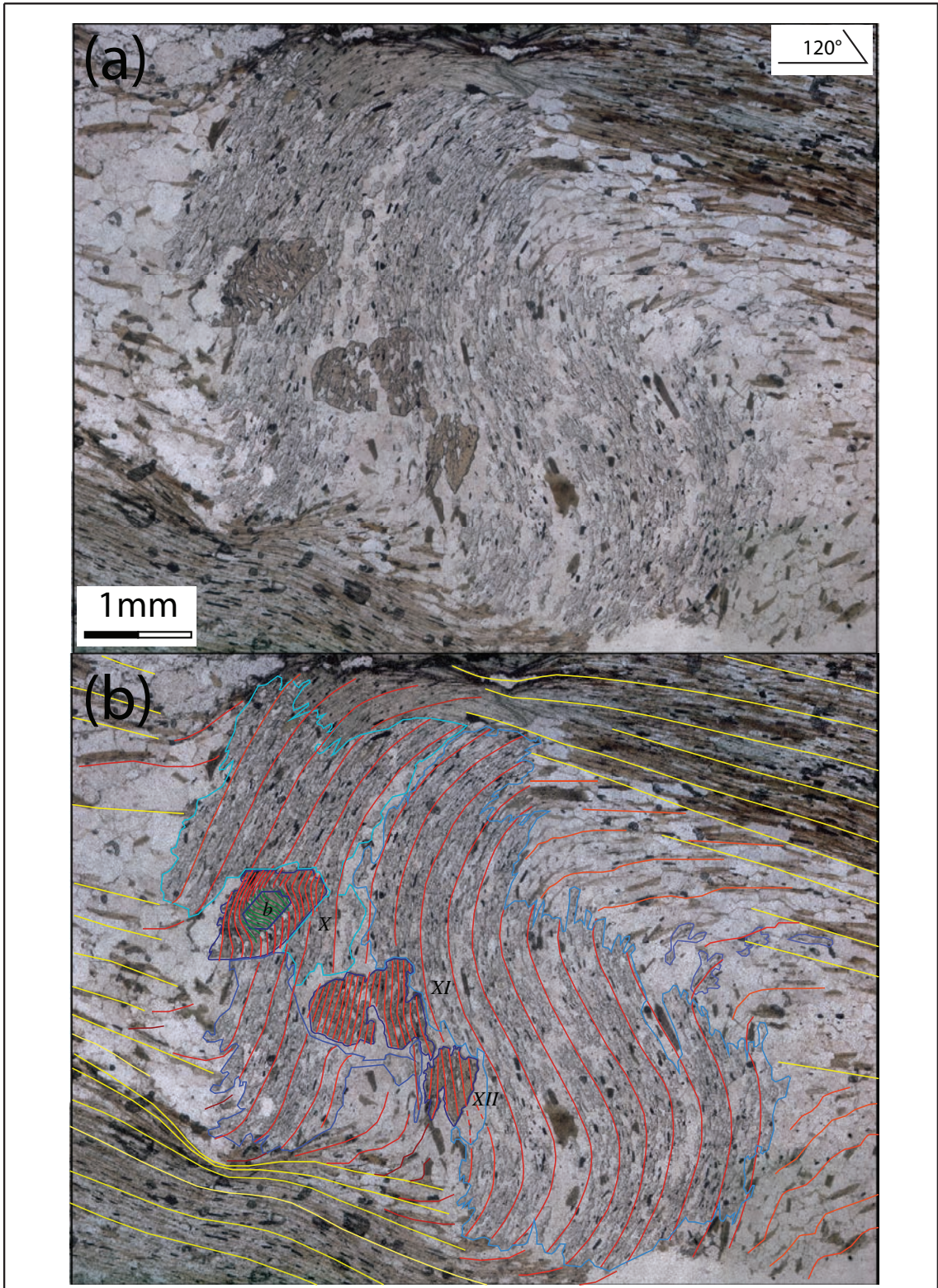


Fig. 4a, b

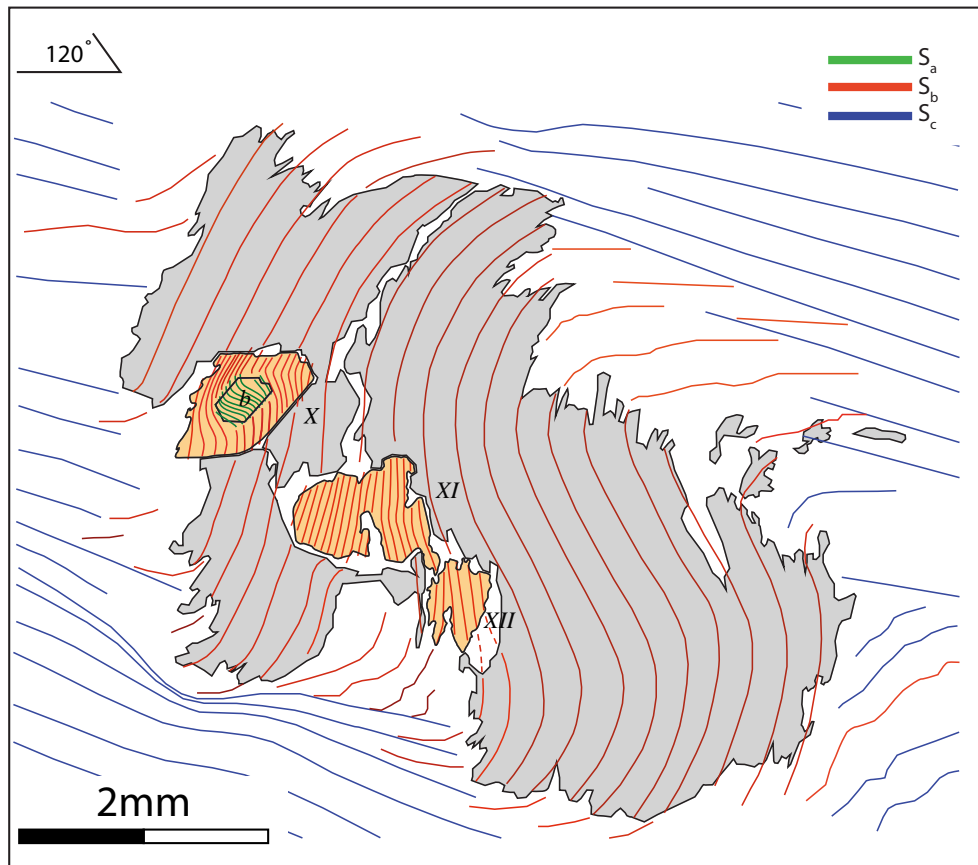


Fig. 4c

**Figure 4:**

Andalusite porphyroblast cluster that has overgrown 3 staurolite porphyroblasts in a vertical thin section striking at 120°.

a) High resolution photo of the whole cluster of porphyroblasts.

b) Line diagram superimposed on (a) of foliations in the matrix, foliation preserved as inclusion trails and the boundaries of porphyroblasts, including differently oriented andalusite crystals within the cluster labelled **IX**. Staurolite porphyroblasts are numbered **X**, **XI** and **XII**.

**X** contains a microstructural core labelled “b”. S<sub>a</sub> is green, S<sub>b</sub> is red, S<sub>c</sub> is yellow and the trend of S<sub>a</sub> axial planes is shown in purple in 1 location.

c) Same line diagram as (b) without the photomicrograph. S<sub>c</sub> is here in blue.

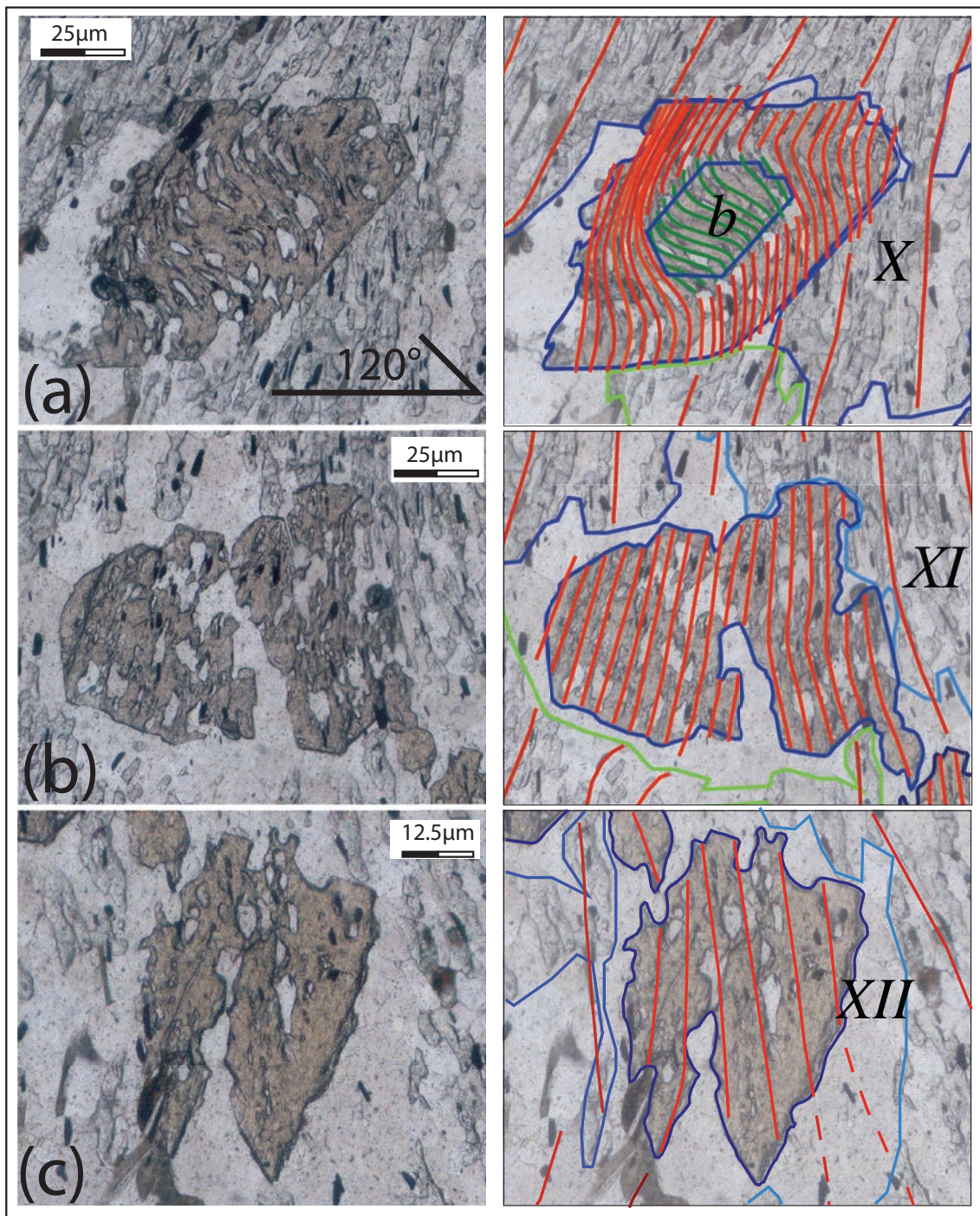


**Figure 5:** Magnified images from Fig. 4 of staurolite porphyroblasts *X*, *XI* and *XII* with inclusion trails overlaid over each photo down the right side. Described in the text.

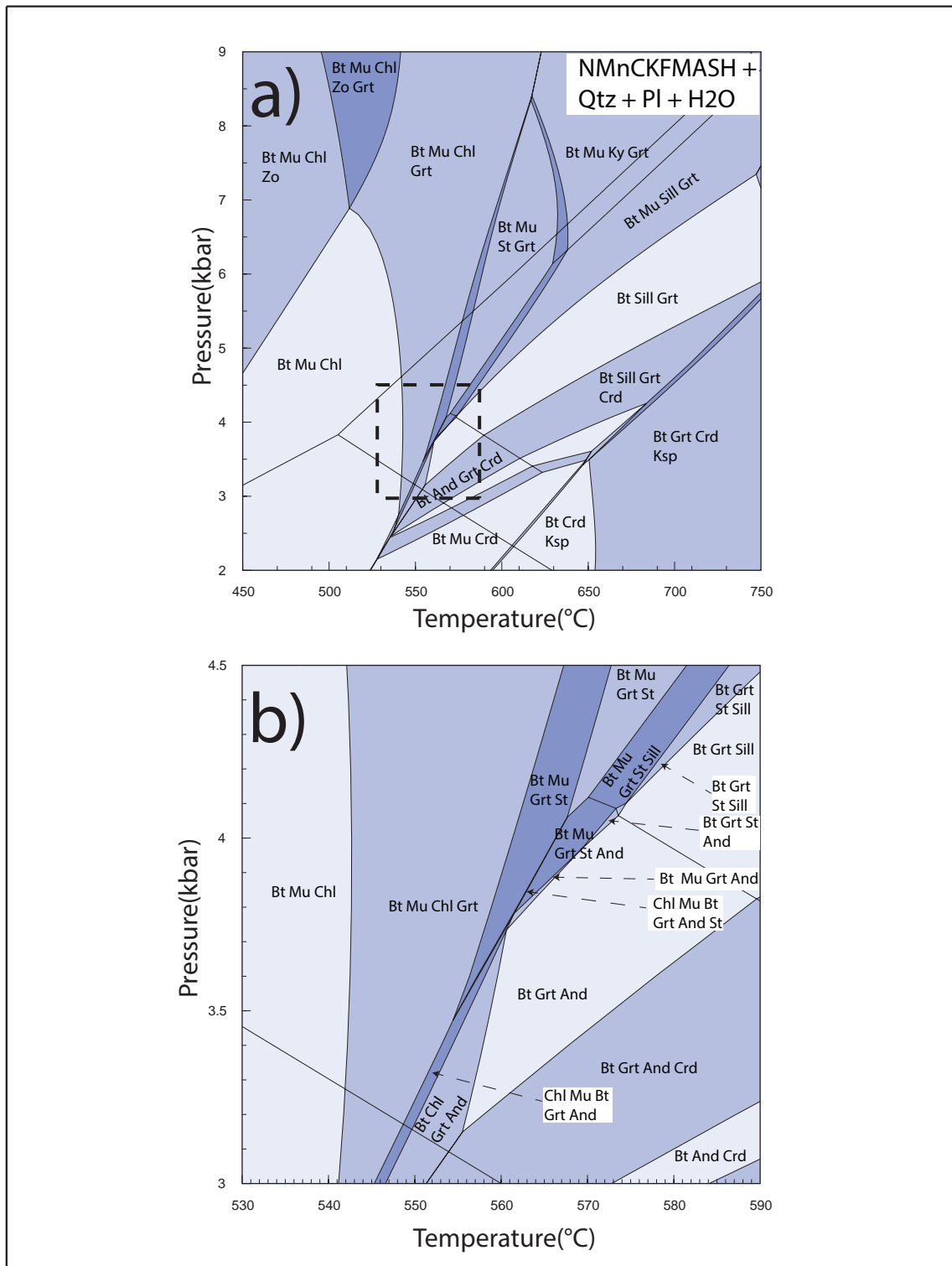


**Figure 6:** (a) shows a Pseudosection of sample 43 in the MnNCKFMASH system.

(b) is a magnification of portion of the pseudosection marked with a rectangle in (a) where staurolite and andalusite coexist.

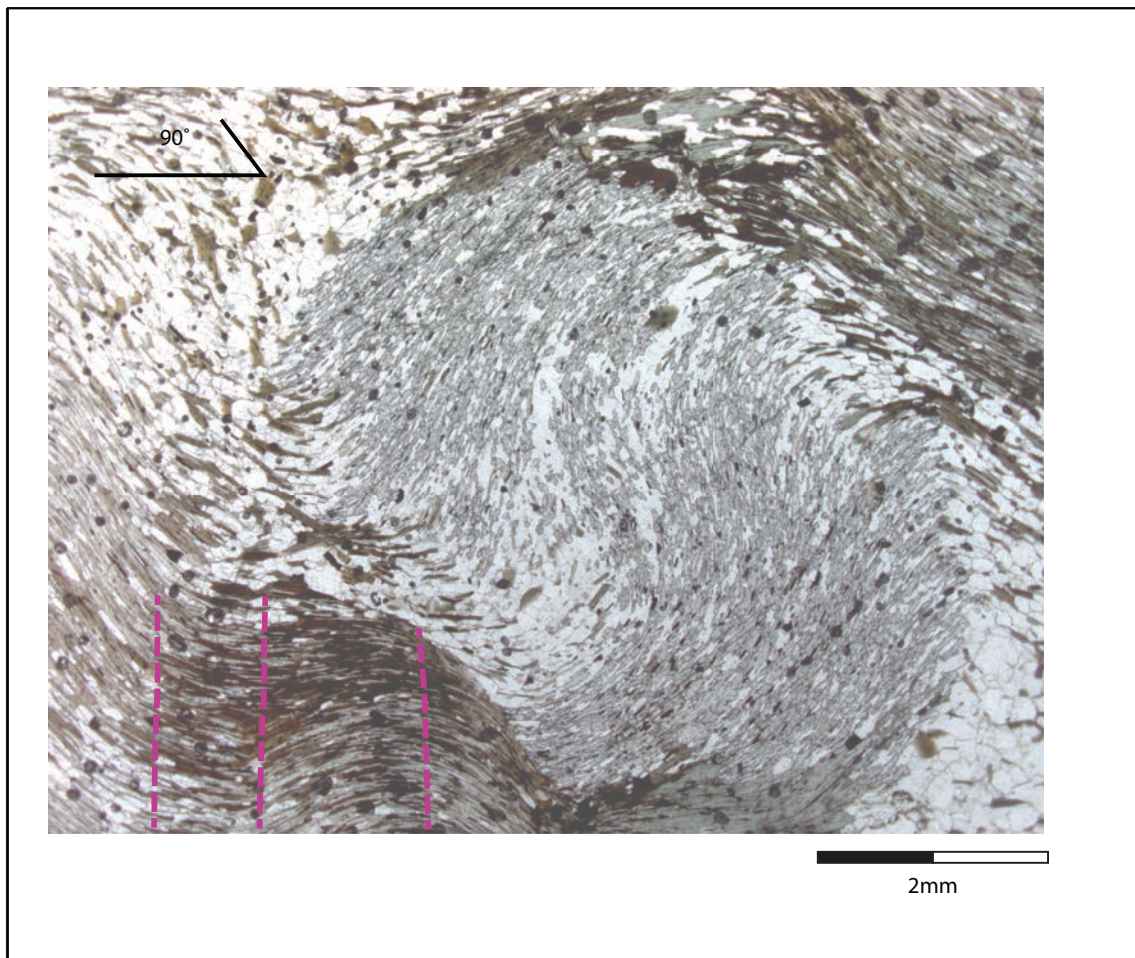


**Figure 7:** Photo of  $S_c$  crenulation axial planes in the vertical section striking at  $90^\circ$  where these crenulations are more obvious than in Figs 2 & 4 because the section is no longer near orthogonal to the crenulation axis.

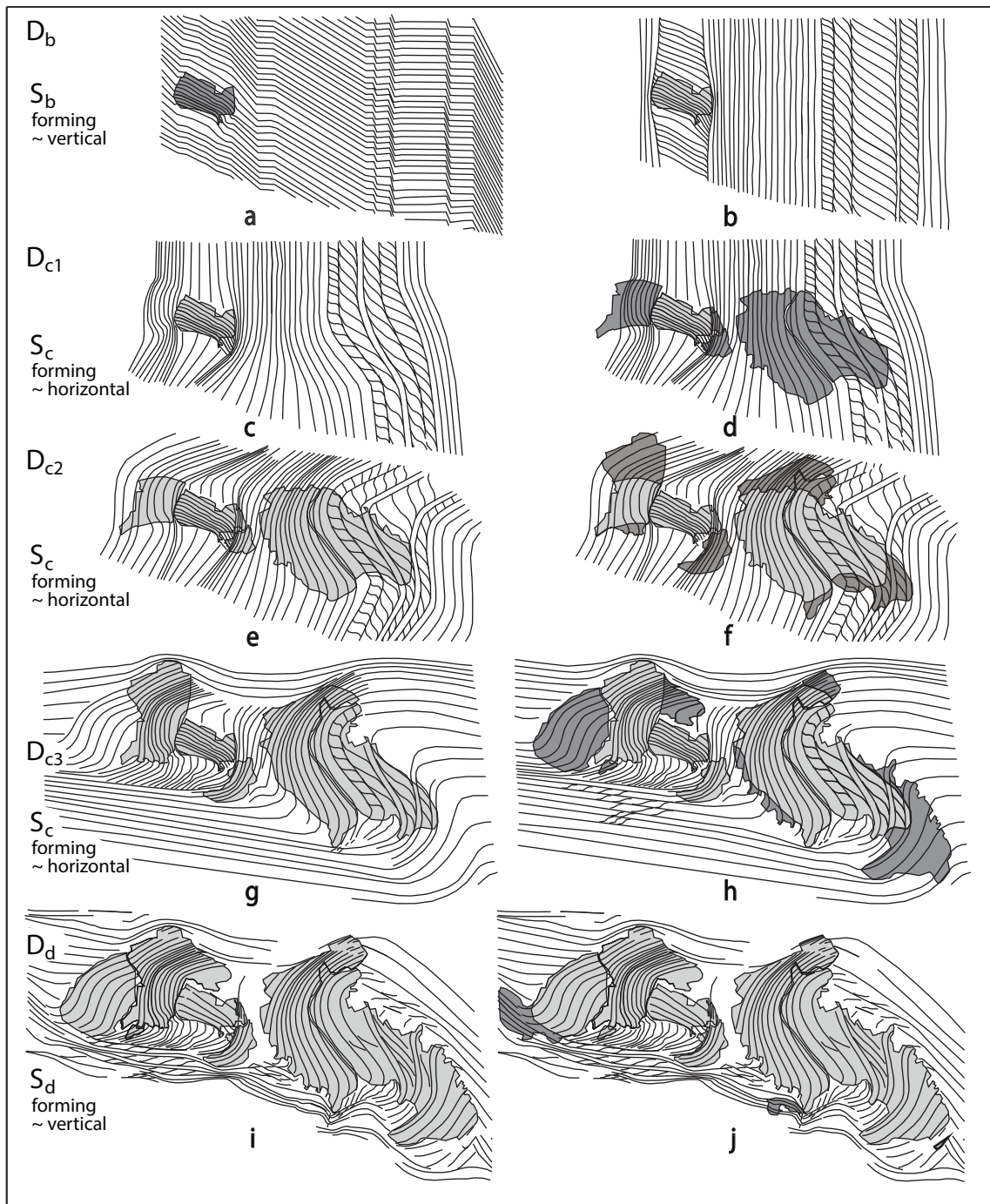


**Figure 8:** Progressive models for inclusion trail development in andalusite clusters *I* and *III* in the vertical section striking at 140° shown in Figs 2, 3a & 3c over 3 deformation events. They are described in detail within the text.

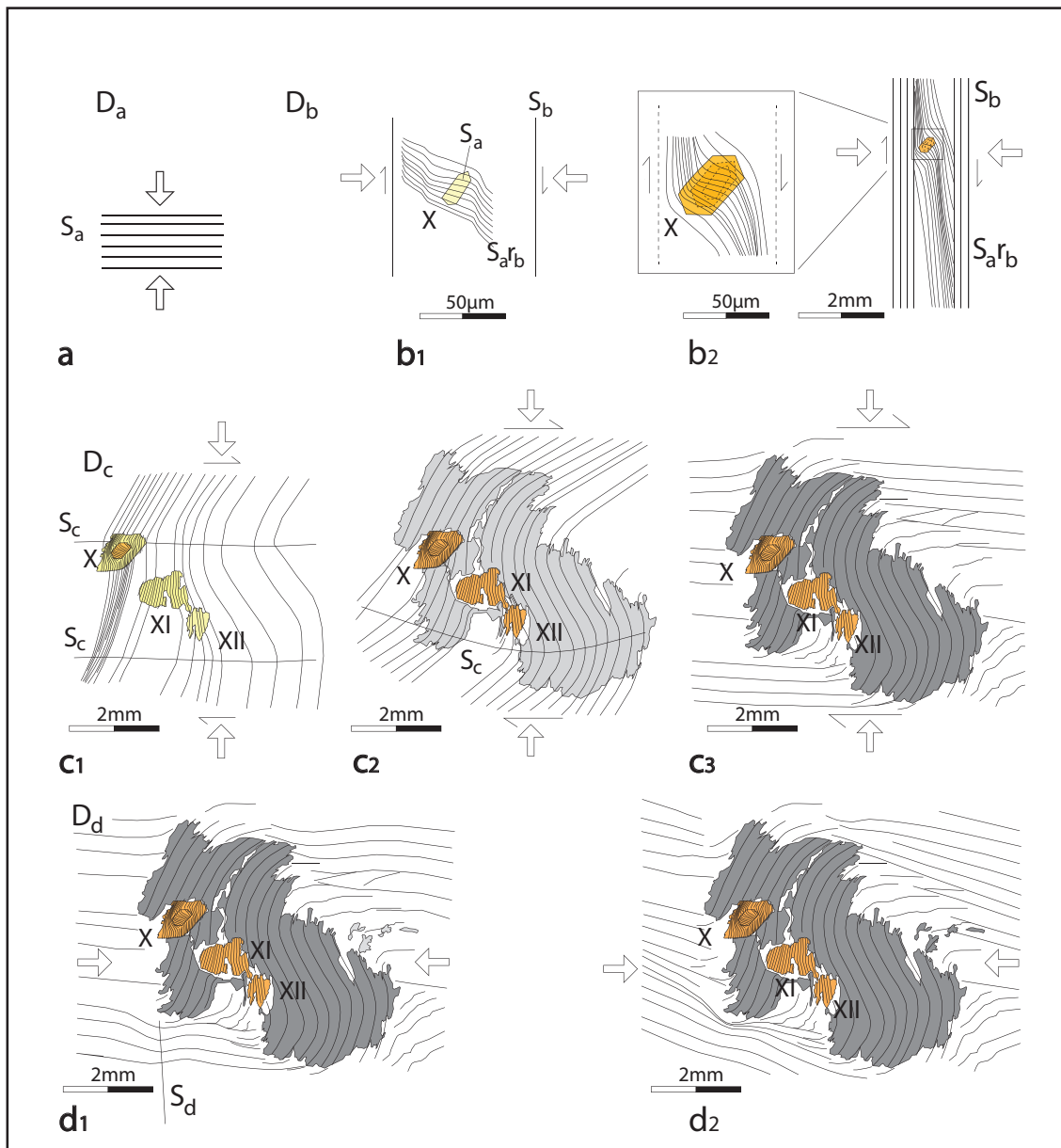


**Figure 9:** Progressive models for inclusion trail development in staurolite and andalusite in the vertical section striking at  $120^\circ$  shown in Figs 4 & 5 over 3 deformation events. They are described in detail within the text.

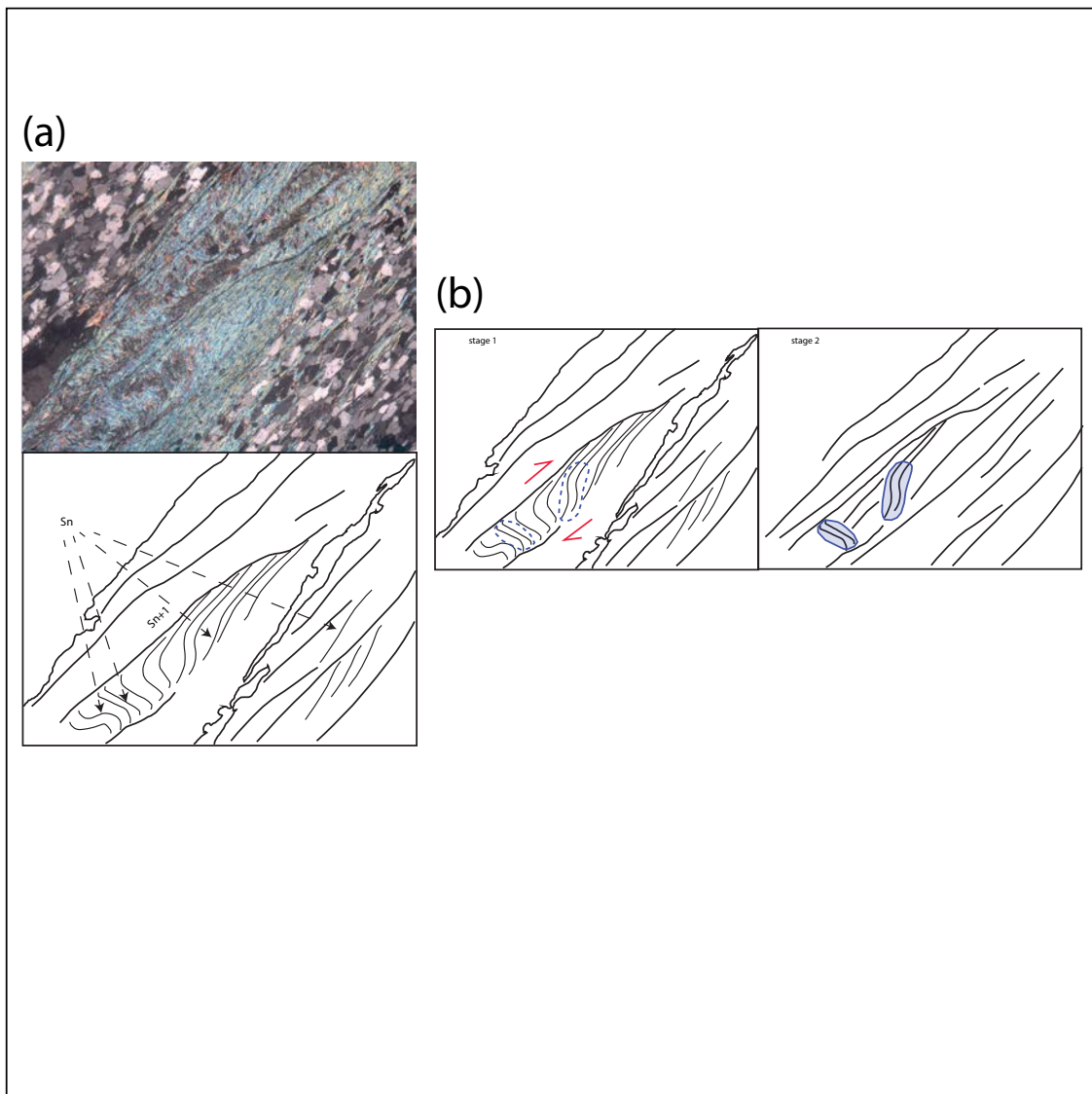


**Figure 10:**

a) Photomicrograph of Himalayan mica-schist (courtesy of M.G. Rubenach) on the top and interpretative line diagram below. The M domain shows an early crenulation cleavage being variably reactivated by a later event.

b) Two stage diagram that illustrates an alternative model for Johnson (2009) "rotated" porphyroblasts. In this model porphyroblasts overgrow the already rotated foliation featured in (a). The final geometry in stage 2 is similar to the one emphasized by Johnson (2009).

**- CHAPTER IV -**

**THE SIGNIFICANCE FOR METAMORPHISM, OROGENESIS AND  
PT PATHS OF ~40 MILLION YEARS OF MULTIPLE PHASES OF  
DEFORMATION AND EFFECTIVELY SYNCHRONOUS  
STAUROLITE-ANDALUSITE GROWTH**

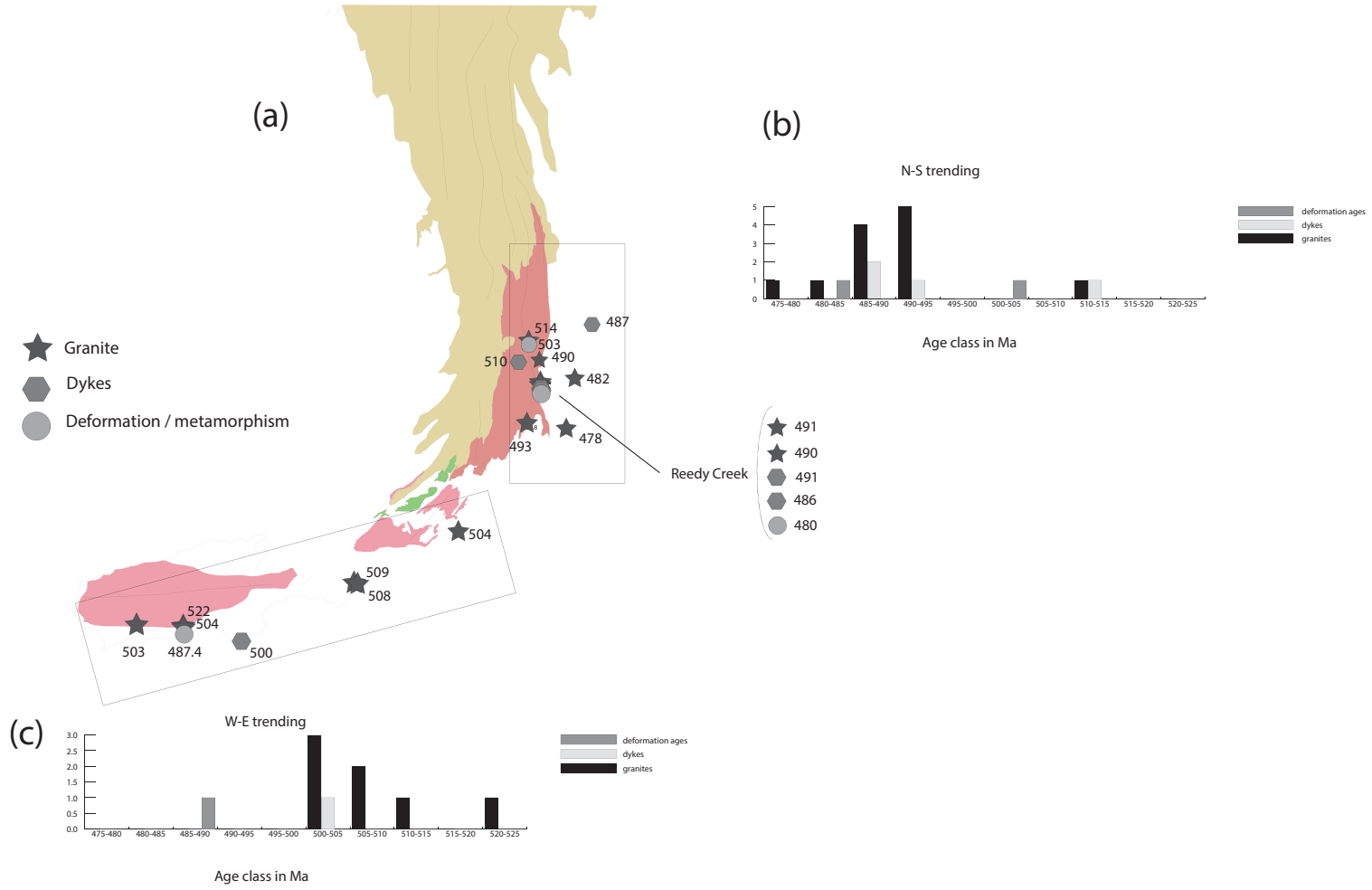


**Figure 1:**

- a) Simplified structural map of the Fleurieu arc with the location, type and age determination derived from the literature.
- b) Histogram of combined ages from the N/S trending portion of the arc.
- c) Histogram of combined ages from the W/E trending portion of the arc.

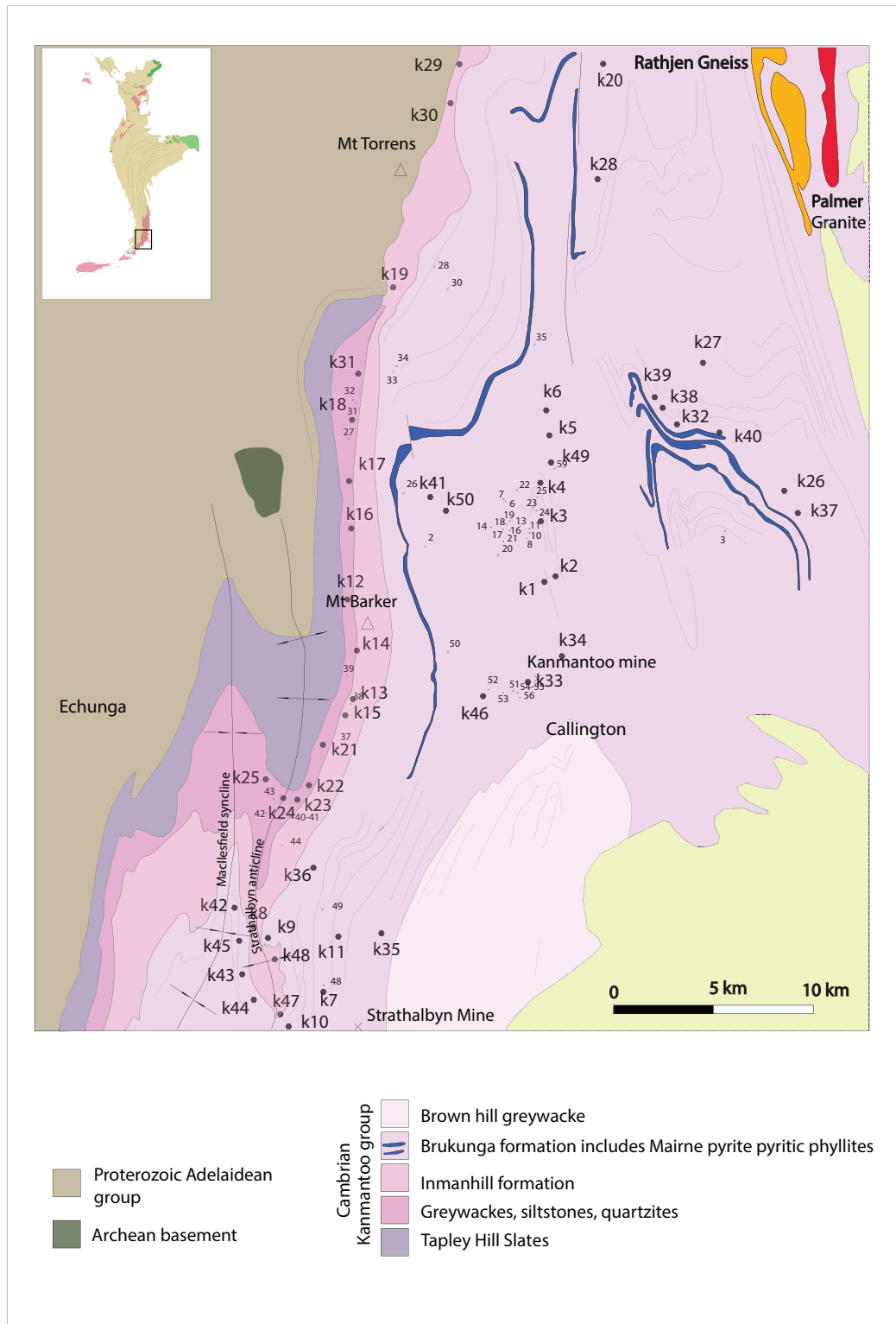


**Figure 2:** Simplified structural map of the study area with samples locations based on 1/50000 maps of “Echunga” and “Milang”. Samples that start with the letter “k” were collected by N.S. Adshead-Bell, samples that do not start by a letter were collected by I.V. Sanislav and A. Ali.

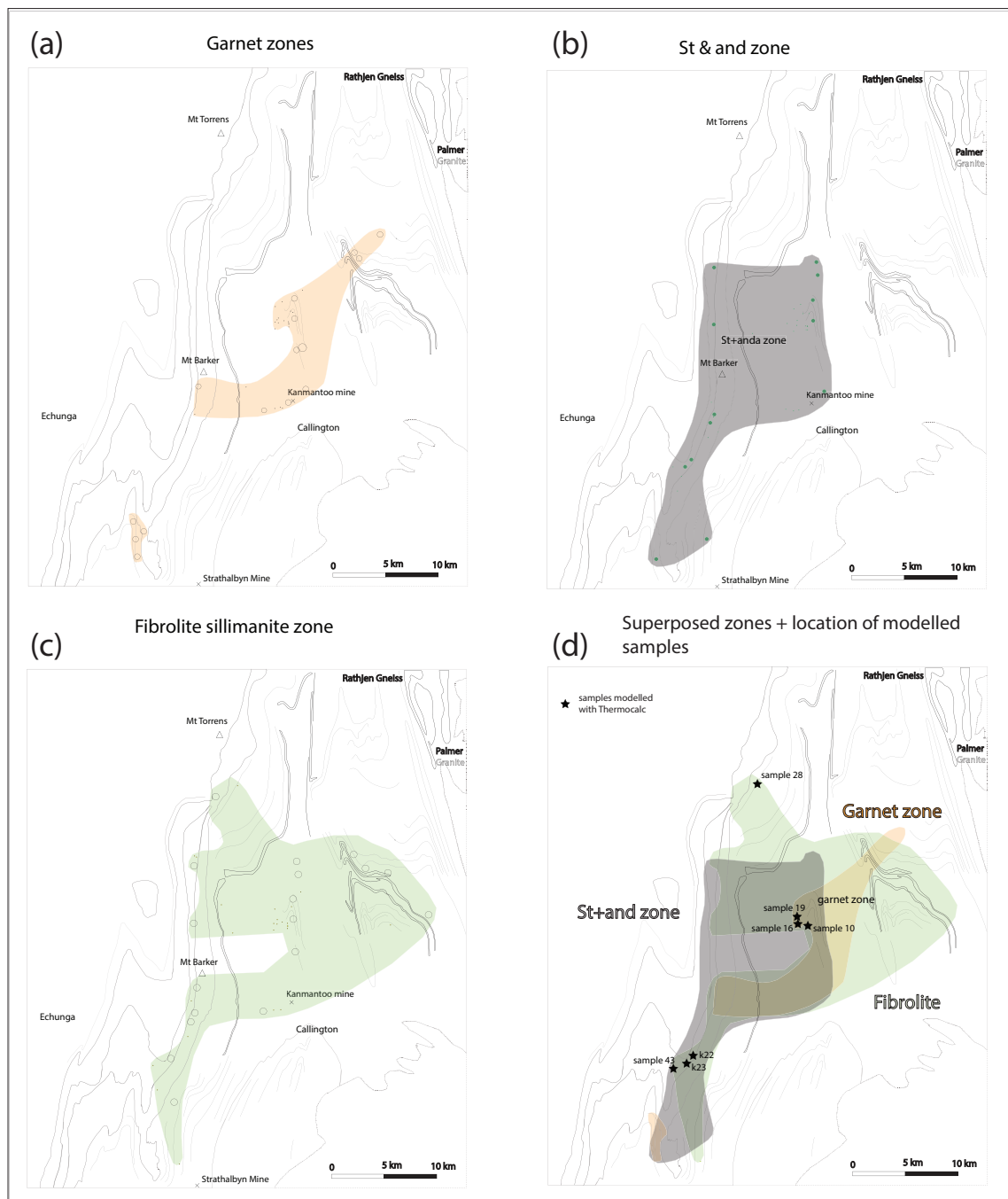


**Figure 3:** Maps of the study area with metamorphic mineral zones:

- Garnet zones.
- Co-stable staurolite and andalusite zone.
- Fibrolite sillimanite zone.
- Combination of all the above maps; the black stars show the location of samples that were modelled with Thermo-calc

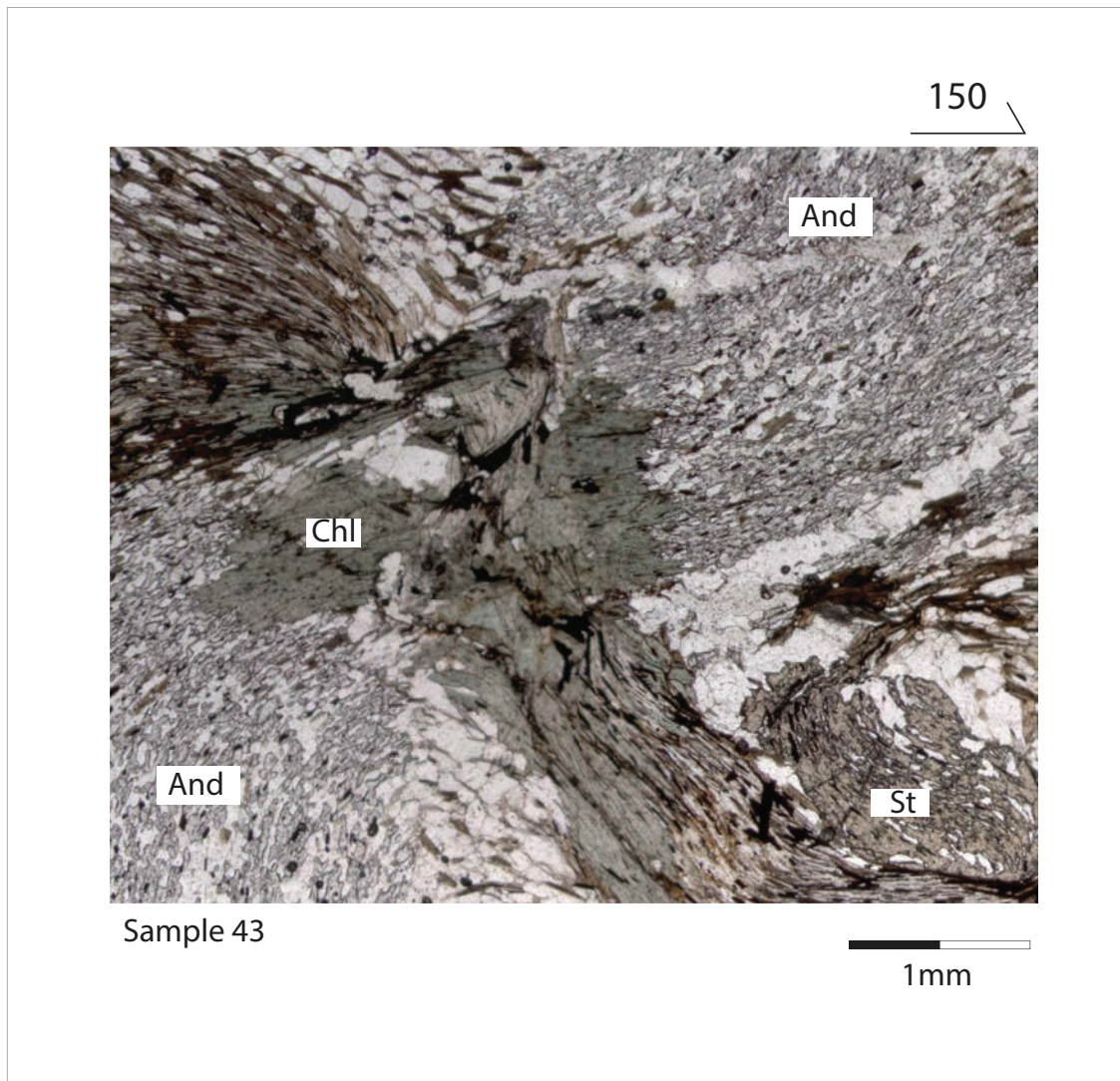


**Figure 4:** Plane polarized photomicrographs of sample 43 showing the textural and spatial relationship between biotite, chlorite and sillimanite. Biotite relics on the top left and adjacent to the staurolite on the bottom right reveal chlorite has replaced biotite that was located between two large poikiloblastic andalusites and possibly some portions of the andalusite rims. Small grains of fibrolitic sillimanite are locally preserved within the biotite and chlorite. Staurolite is present on the bottom right hand side. Plane polarized light.

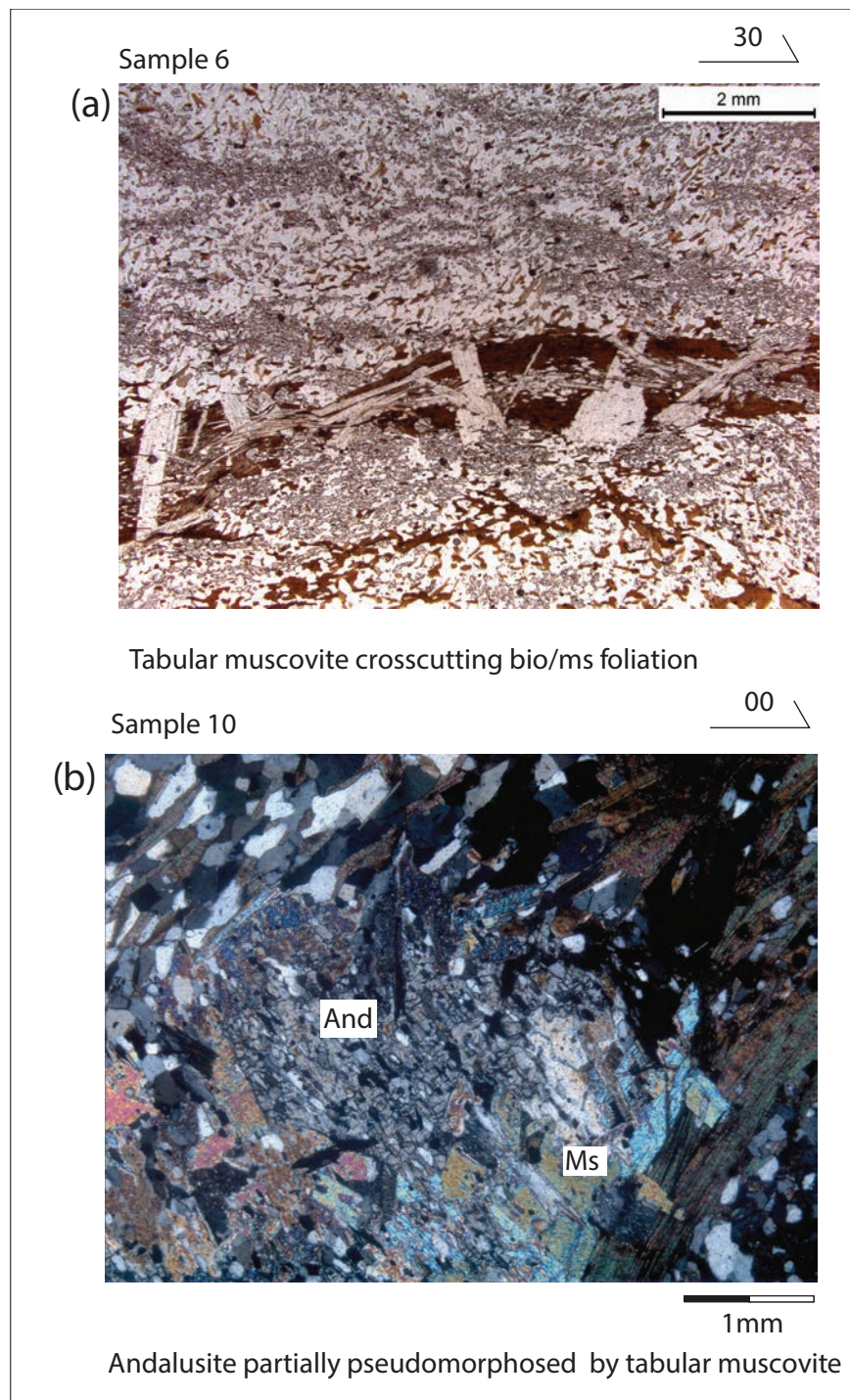


**Figure 5:**

- a) Photomicrograph in plane polarized light of sample 6. It shows poikiloblastic andalusite and coarse muscovite cross-cutting muscovite biotite foliation.
- b) Photomicrograph in plane polarized light of sample 10. It shows poikiloblastic andalusite partially pseudomorphed by coarse muscovite.

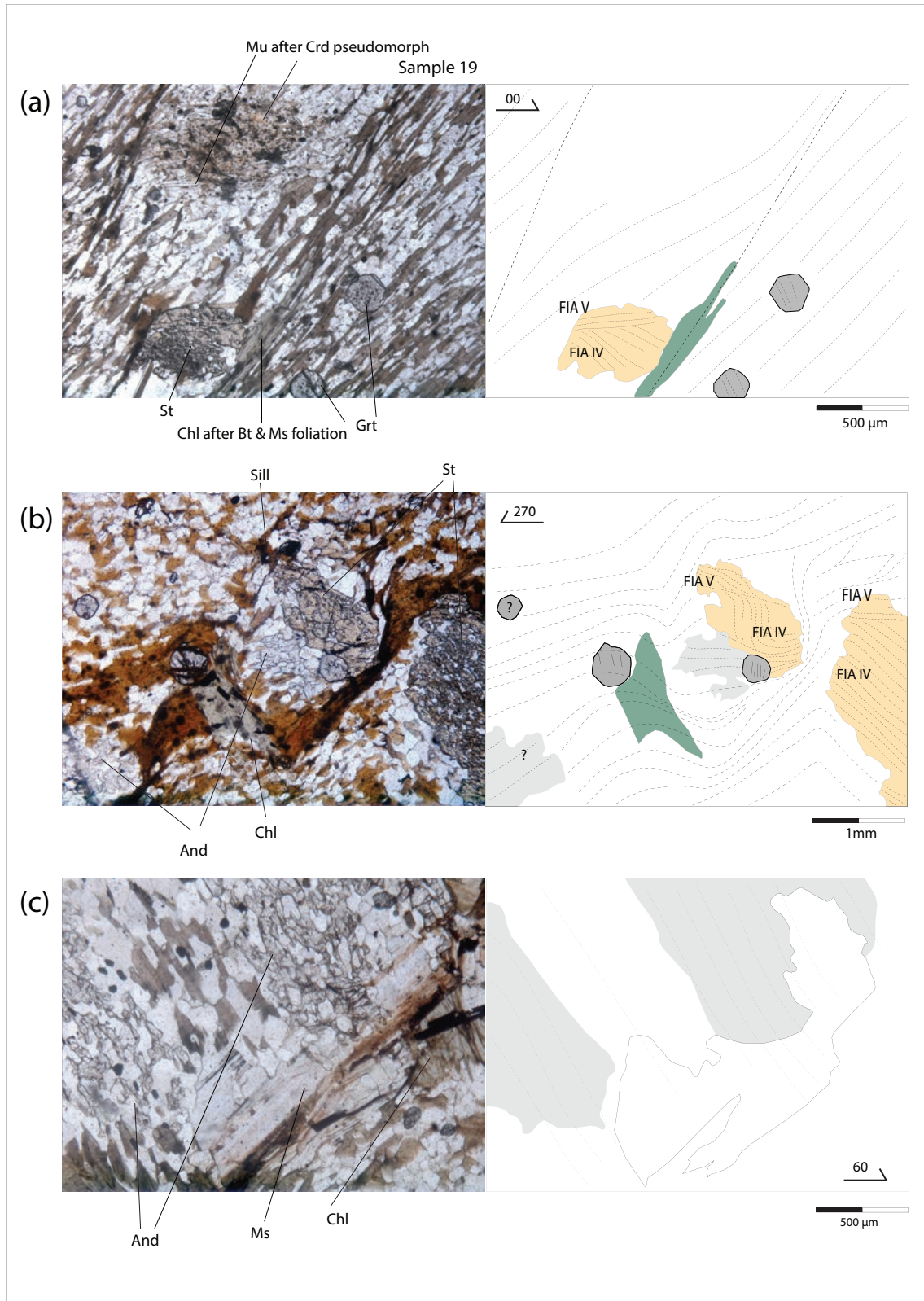


**Figure 6**

Plane polarized photomicrographs of sample 19

- a) Cordierite porphyroblast relic with relics of steeply north pitching foliation as inclusions is pseudomorphed by muscovite. Small garnets contain sub-vertical foliation. Staurolite contains gently north pitching foliation curving ACW into and truncated by truncated by sub-horizontal crenulation cleavage. The latter is slightly curving ACW towards the margin of the porphyroblast and truncated by the matrix foliation. The curvatures of the staurolite core asymmetries define a FIA IV whereas the rim ones define a FIA V. The latter is locally overgrown by late chlorite.
- b) Small garnet porphyroblasts contain sub-vertical fine grained-foliation truncated by sub-horizontal foliation. Staurolite core contains similar fine-grained steep foliation curving ACW into sub-horizontal foliation in rim. Complete truncation of the adjacent garnet in rim by sub-horizontal foliation below suggests it predates staurolite core, but it may have grown in the same event. Sub-horizontal foliation in staurolite rim curves gently CW on right side of garnet and on left where it is coarser grained and preserved within andalusite. The latter indicates the andalusite grew later, possibly later in same sub-vertical foliation event that eventually truncated the sub-horizontal foliation in the staurolite rim and the andalusite. This sub-vertical foliation curves CW into sub-horizontal matrix foliation. The inclusion trails asymmetries of the staurolite cores define a FIA IV and the asymmetries of staurolite rims and andalusite a FIA V. Later fibrolitic sillimanite grows around biotite. Chlorite postdates all other phases.
- c) Coarse tabular muscovite grown across matrix has grown against and includes but appears to not have replaced a portion of the poikiloblastic andalusite on its left. Biotite is locally replaced by random late chlorite.

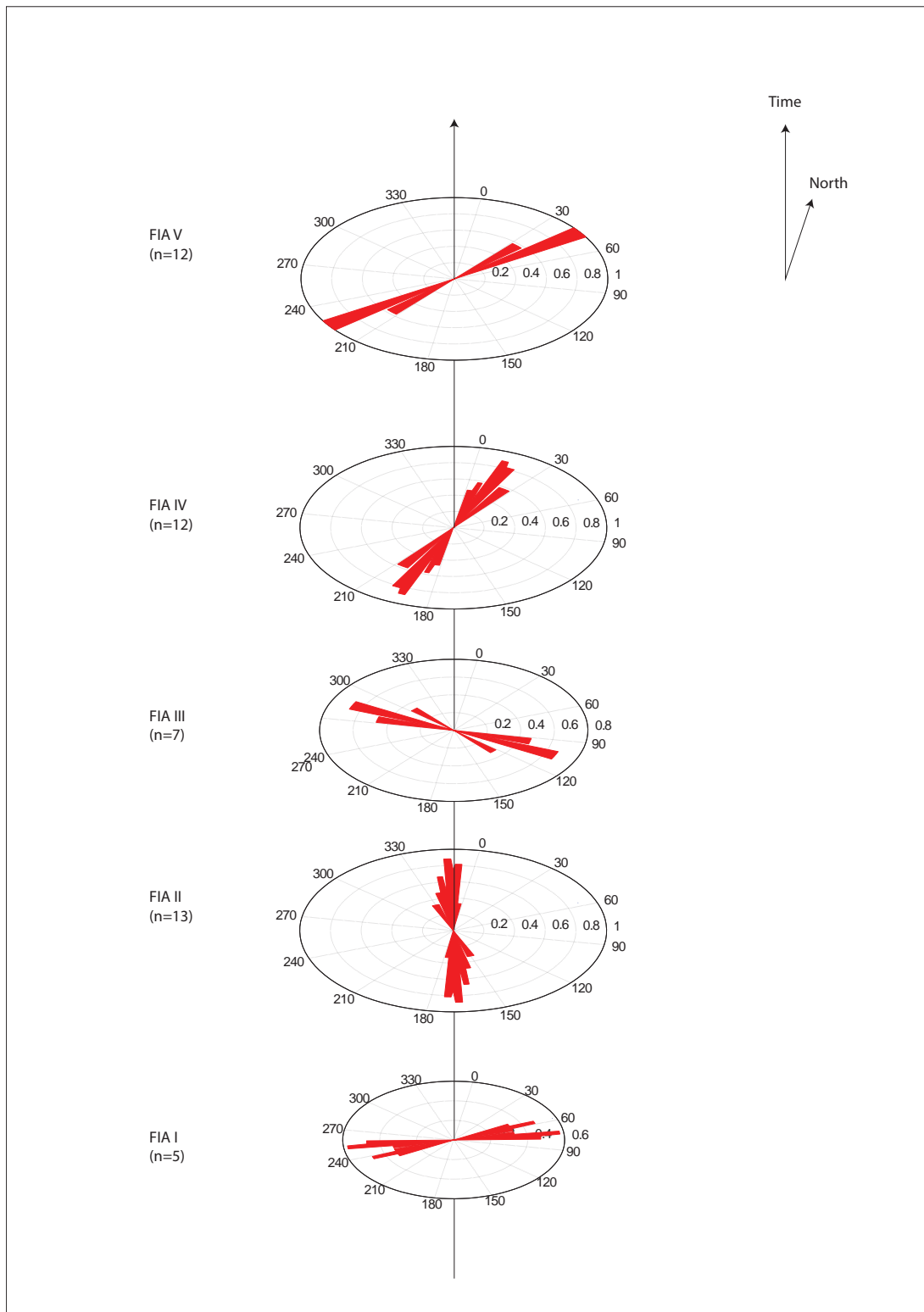


**Figure 7:** 3D representation of the succession of foliation intersection/inflexion axes measured from the Kanmantoo porphyroblastic rocks. Each rose diagram was plotted using M.A.R.D (moving average rose diagram) Matlab code (Munro & Blenkinsop, 2012).

Sample	Porphyroblast/ symptomatic mineral phases	FIA	CaO bulk composition in molar %
10	Grt And St	V II → III III	0.47 %
16	And(core/rim) St	II II	1.65 %
19	Crd Grt And St	unknown V IV → V	1.41 %
28	Sill, Ksp, Mu	N/A	0.58 %
43	And St	IV IV	1.679 %
59	Crd Grt And	unknown unknown V	1.77 %
k22	And St	IV IV	0.78 %
k23	And St	IV IV	1 %

**Figure 8:** Table of the porphyroblastic and other main metamorphic phases, FIAs present and calcium molar proportion for each modelled sample.

Sample	Fe2O3	SiO2	Al2O3	TiO2	MnO	CaO	P2O5	SO3	MgO	K2O	Na2O	LOI	BaO	Sum
10 *	9.16	65	15	0.67	0.12	0.47	0.16	0.012	3.25	3.11	1.89	1.07	<0.01	99.912
16 *	8.35	57.85	19.48	0.82	0.14	1.65	0.14	0.017	4	4.17	1.5	1.68	0.1	99.897
19 *	6.95	62.99	17.52	0.73	0.16	1.41	0.16	0.012	3.33	2.61	3.01	1.03	<0.01	99.912
28 *	7.46	59.32	18.97	0.78	0.08	0.58	0.09	0.02	3.83	5.56	1.51	1.53	0.1	99.83
43 †	7.777	59.505	18.794	0.762	0.09	1.679	0.182	0.0178	3.819	3.557	2.248	1.31		99.7408
59 *	6.84	64.51	16.05	0.75	0.09	1.77	0.17	0.01	3.8	2.73	1.97	1.2	0.07	99.96
k22 †	7.54	62.39	17.35	1.165	0.047	0.64	0.228	0.026	3.014	4.607	0.777	0.14		97.924
k23 †	9.16	60.49	18.89	1.192	0.058	0.82	0.245	0.017	3.289	3.958	0.746	0.162		99.027

\* Samples analysed at Amtas Bureau Veritas  
† Samples analysed at JCU Advance Analytical centre

**Figure 9:** Table of the bulk chemistry composition obtained by X-Ray fluorescence for 8 samples. Major elements are here in weight %.

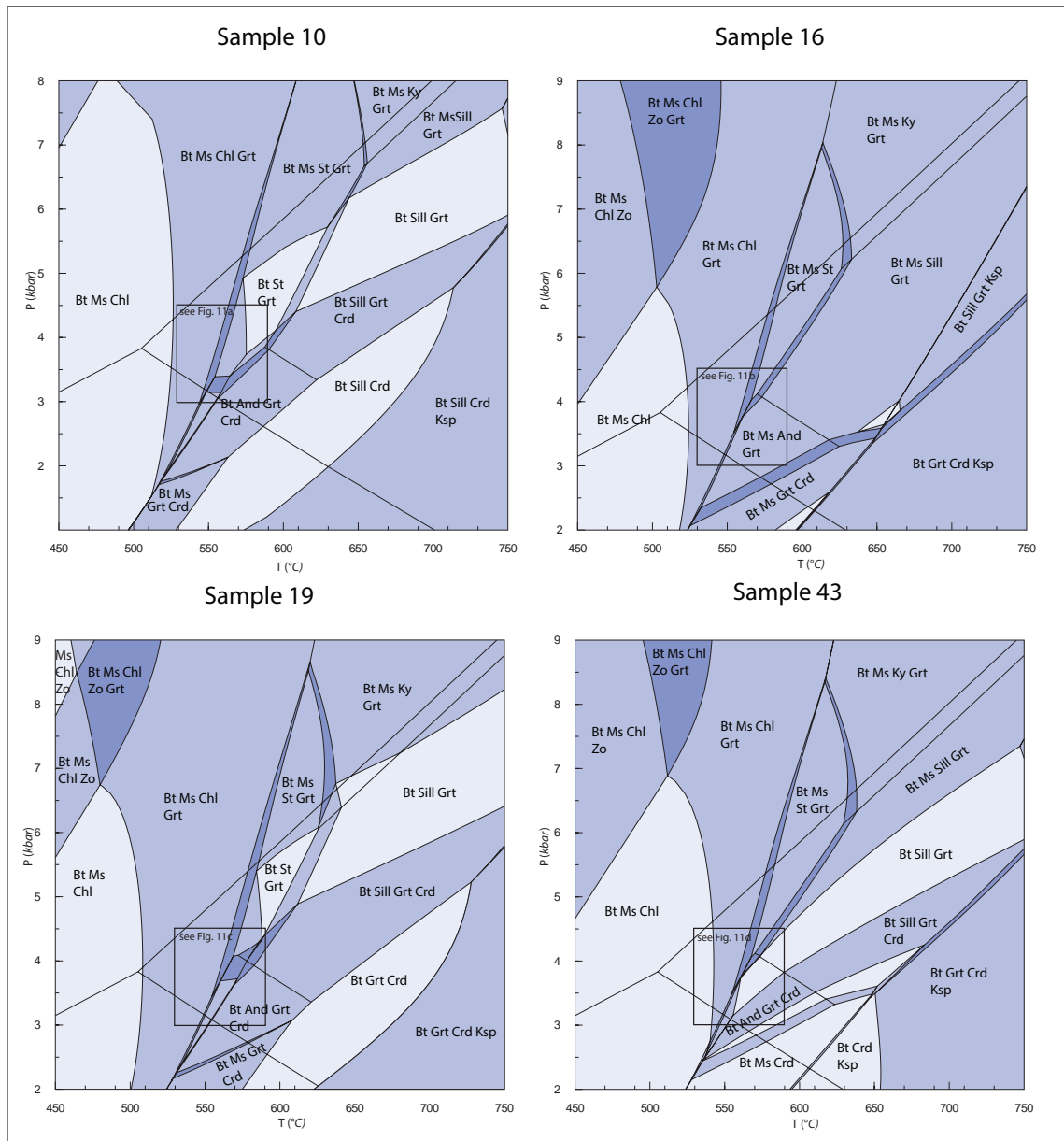


Fig. 10a

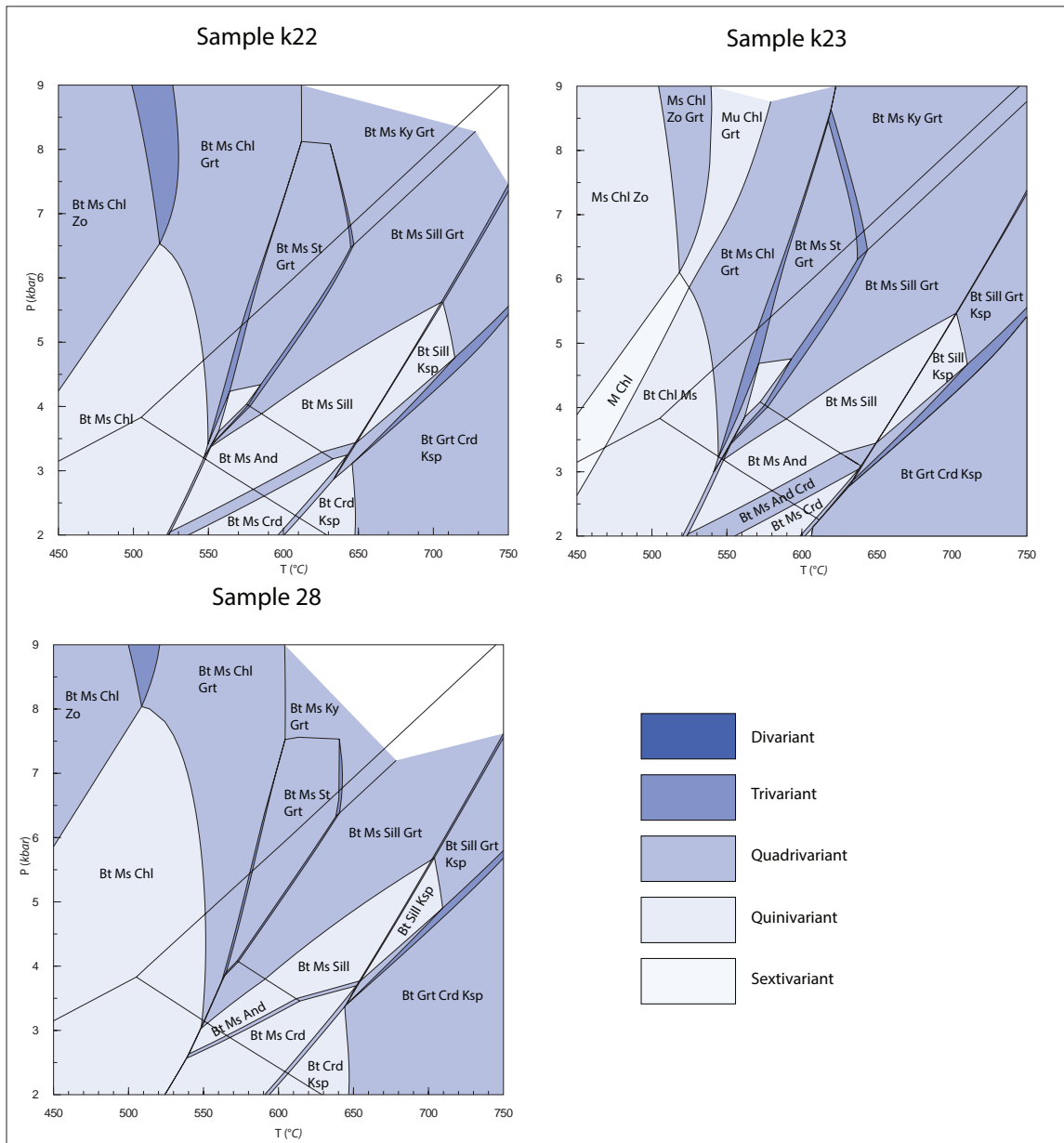


Fig. 10b

**Figure 10:**

- a) Modelled pseudosections for samples 10, 16, 19 and 43. Increasing shades of blue indicates increased variance.
- b) Modelled pseudosections for samples k22, k23, 28. Increasing shades of blue indicates increased variance.



**Figure 11:** Shows a magnified portion of the T-P fields from Fig. 10 where staurolite and andalusite co-exist in Thermocalc for successively sample 10 (a), sample 16 (b), sample 19(c), sample 43 (d), sample k22 (e) and sample k23 (f).

The specific stability fields for staurolite and andalusite for each sample was then extracted from (a), (b), (c), (d), (e), (f) and plotted on a single T-P diagram (g). The overall range of temperature and pressure that thermo-calc modelled for this assemblage and samples is 30°C and 1kbar (g).

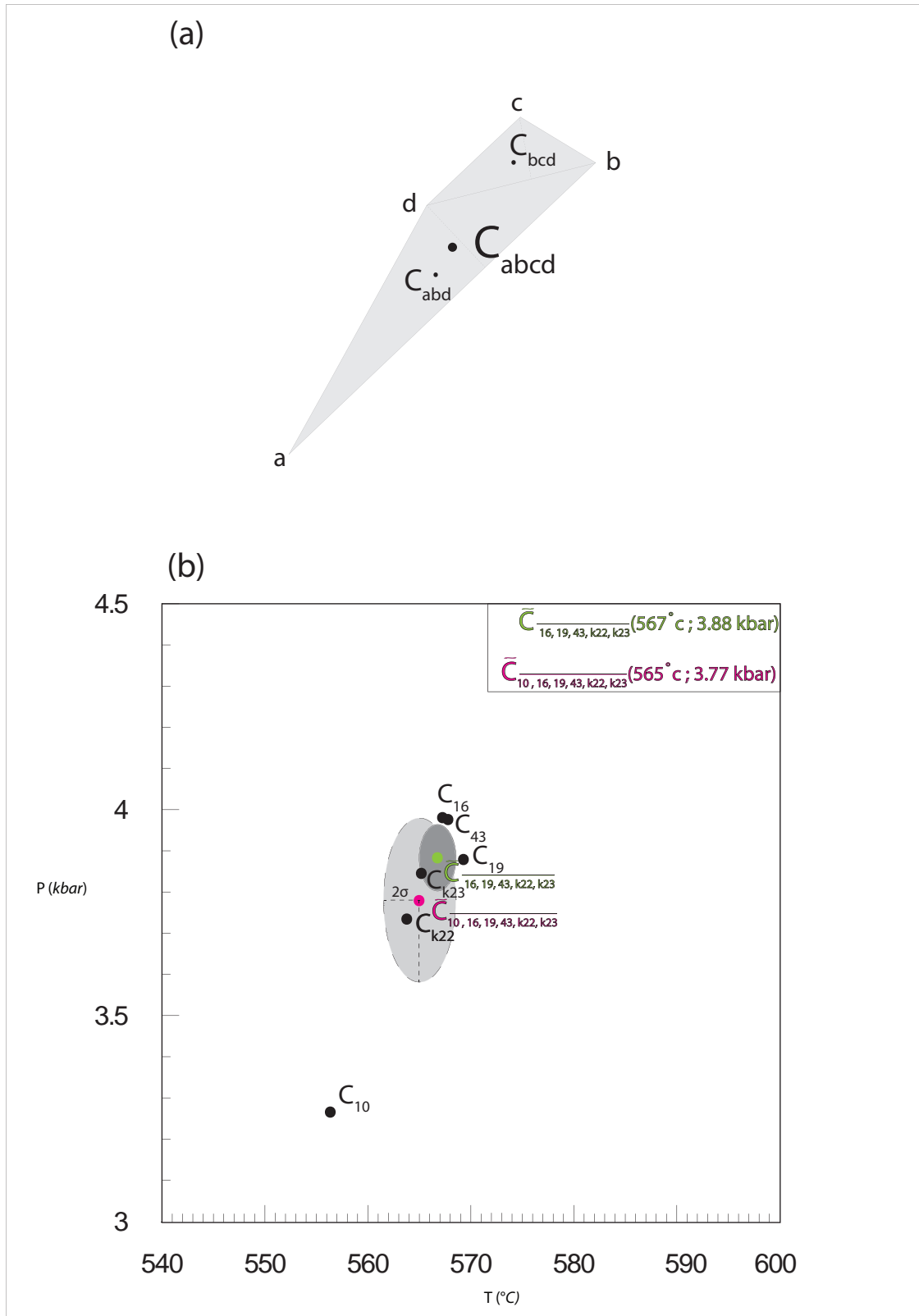


**Figure 12:** Shows the graphical centroid method used to determine the average T-P from Fig. 11g. This consists of dividing the polygon shaped field for one sample into individual triangles to find its centroid (a) and then averaging the T & P values of the centroid for each sample (b). Since C10 is discordant compared to the others, two average centroids were calculated C10, 16, 19, 43, k22, k23 and C16, 19, 43, k22, k23. The ellipsoid around the two average centroids correspond to  $2\sigma$  variance in T & P.

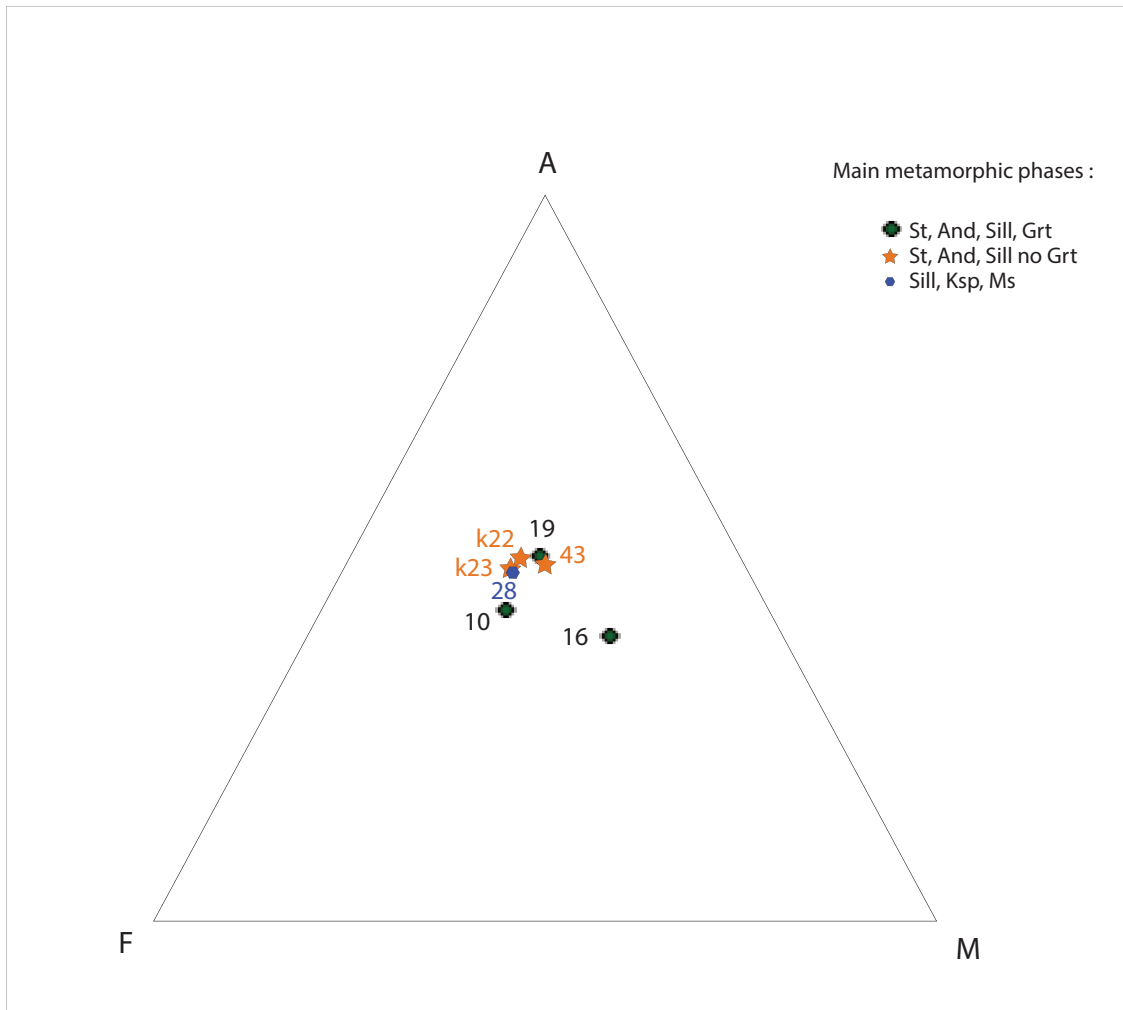


**Figure 13:** Shows the relative molar proportions of aluminium, iron, magnesium and the main mineralogical phases for the modelled samples.

molar %	Samples with St & And			Samples with St, And & Grt		
	K22	K23	Sample 43	Sample 10	Sample 16	Sample 19
SiO <sub>2</sub>	70.74	68.85	66.78	71.76	65.54	69.71
Al <sub>2</sub> O <sub>3</sub>	11.59	12.67	12.43	9.76	12.01	11.43
CaO	0.78	1.00	2.02	0.56	2.00	1.67
MgO	5.09	5.58	6.39	5.35	6.76	5.49
FeO	6.43	6.99	6.57	7.61	7.12	5.79
K <sub>2</sub> O	3.33	2.87	2.55	2.19	3.01	1.84
Na <sub>2</sub> O	0.85	0.82	2.45	2.02	1.65	3.23
MnO	0.05	0.06	0.09	0.11	0.13	0.15

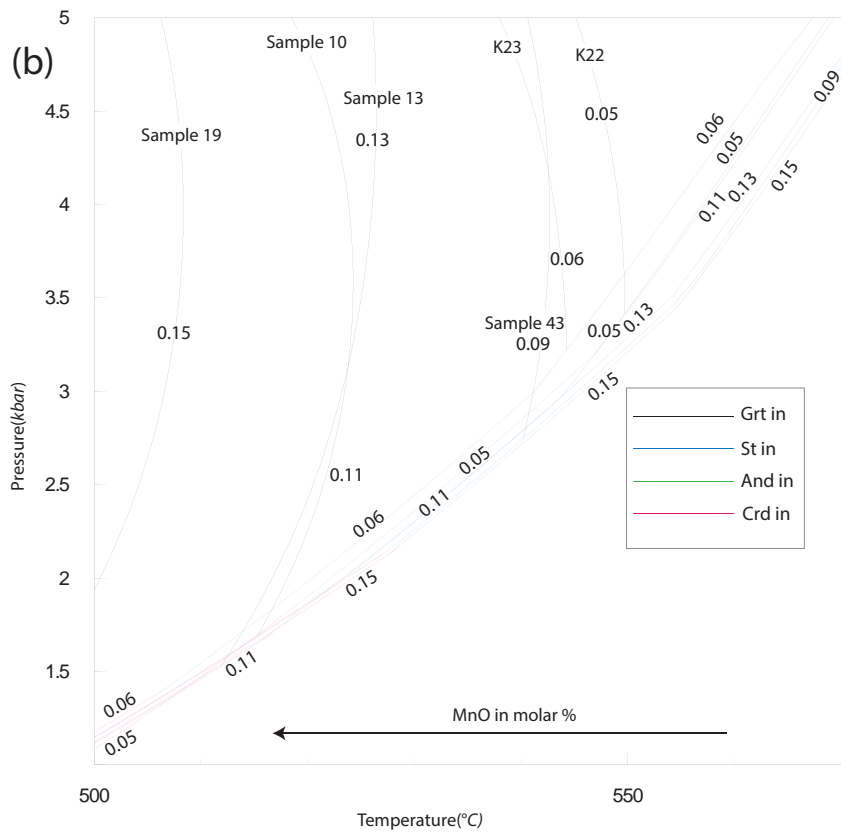


**Figure 14:**

(a) table of relative molar proportion of major elements of samples used for Thermocalc. The green rectangle contains samples bearing staurolite and andalusite but no garnet. The blue rectangle shows samples containing staurolite, andalusite and garnet.

(b) The mineral in-lines computed with Thermo-calc for samples 10, 13, 19, 43, k22 and k23. The in-lines are garnet black, staurolite blue, andalusite green and cordierite red. The numbers plotted on to the line correspond to their MnO molar proportion. This figure shows that the St, And, Crd in-lines are tightly clustered, not changing much with differing manganese contents. However, for garnet in-lines, the lower the manganese content (lower MnO %), the higher the temperature of the Grt in-line.



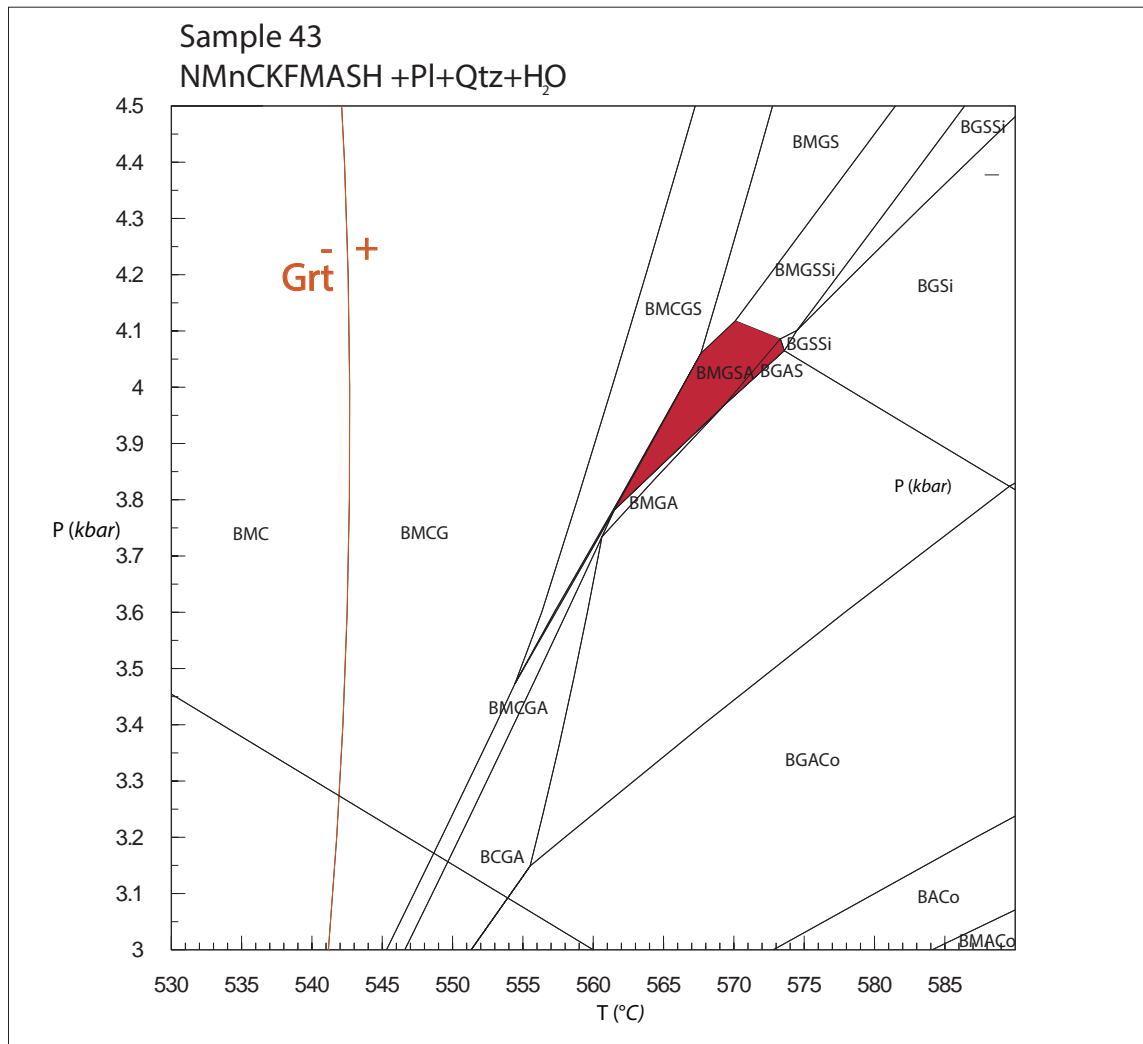
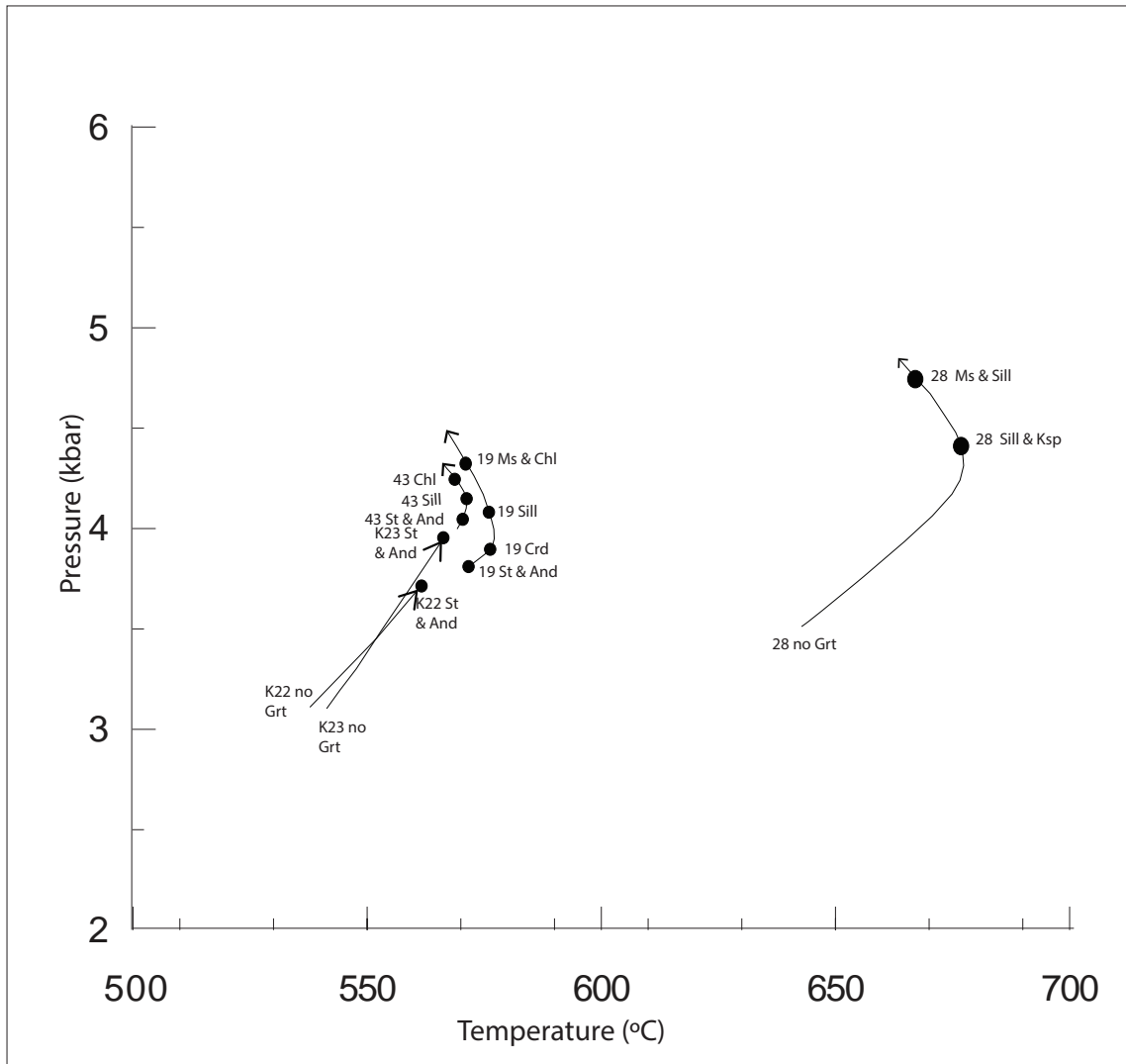


Fig. 15c

**Figure 15:**

Pseudosections (a), (b) and (c) from Figs 11e, 11f and 11d for samples k22, k23 and 43 respectively, showing the complexity of their garnet in lines (in orange) relative to the staurolite + andalusite fields (in red). For clarity, the minerals in each zone have been simplified to their initials except for sillimanite (Si) and cordierite (Co). The P-T trajectory marked by a dashed line in (a) and (b) will cause growth of staurolite and andalusite without garnet having grown previously. This is not possible for (c) except no garnet is present in sample 43, suggesting that the pseudosection is not correct. The gross similarity between all 3 pseudosections and the same mineralogy suggests the true pseudosection for 43 is more like (a) or (b) in which case a PT path that could grow andalusite and staurolite synchronously would be like that shown in (a) and (b).



**Figure 16:** Combined PT paths from all samples.